Gaopeng Xu[1], Ping Chang[1,2], Sanjiv Ramachandran[1], Gokhan Danabasoglu[3], Stephen Yeager[3], Justin Small[3], Qiuying Zhang[1], Zhao Jing[4,5], Lixin Wu[4,5]

[1]Department of Oceanography, Texas A&M University, College Station, Texas, USA

[2]Department of Atmospheric Sciences, Texas A&M University, College Station, Texas, USA

[3]National Center for Atmospheric Research, Boulder, Colorado, USA.

[4]Laboratory for Ocean Dynamics and Climate, Qingdao Pilot National Laboratory for Marine Science and Technology, Qingdao, China.

[5]Key Laboratory of Physical Oceanography, Ministry of Education/Institute for Advanced Ocean Study/Frontiers Science Center for Deep Ocean Multispheres and Earth System (DOMES)/College of Oceanic and Atmospheric Sciences, Ocean University of China, Qingdao, China

Corresponding author: Gaopeng Xu (gaopxu@tamu.edu)

Key Points:

- SST biases are considerably reduced in high-resolution models compared to low-resolution models
- Nonlocal KPP mixing is an important factor in SST bias reduction
- Eddy vertical heat transport can modulate nonlocal KPP mixing in eddy-active regions

Abstract

Impacts of model horizontal resolution on sea-surface temperature (SST) biases are studied using high-resolution (HR) and low-resolution (LR) simulations with the Community Earth System Model (CESM) where the nominal resolutions are 0.1° for ocean and sea-ice and 0.25° for atmosphere and land in HR, and 1° for all component models in LR, respectively. Results show that, except within eastern boundary upwelling systems, SST is warmer in HR than LR. Globally averaged surface ocean heat budget analysis indicates that 1°C warmer global-mean SST in HR is mainly attributable to stronger nonlocal vertical mixing and shortwave heat flux, with the former prevailing over the latter in eddy-active regions. In the tropics, nonlocal vertical mixing is slightly more important than shortwave heat flux for the warmer SST in HR. Further analysis shows that the stronger nonlocal mixing in HR can be attributed to differences in both the surface heat flux and shape function strength used in the parameterization. In addition, the shape function shows a nonlinear relationship with surface heat flux in HR and LR, modulated by the eddy-induced vertical heat transport. The stronger shortwave heat flux in HR, on the other hand, is mainly caused by fewer clouds in the tropics. Finally, investigation of ocean advection reveals that the improved western boundary currents in HR also contribute to the reduction of SST biases in eddy-active regions.

Plain Language Summary

Sea-surface temperature (SST) is a key climate variable, through which the atmosphere and ocean are coupled. However, current generation climate models that have nominal horizontal resolutions of ~1° generally produce colder-than-observation SST over much of the tropics and midlatitudes. Increasing model resolution to 0.25° or finer can help reduce this cold bias, but the underlying physics is not well understood. By analyzing high-resolution (HR) and low-resolution (LR) Community Earth System Model (CESM) simulations, we find that vertical turbulent processes, particularly the convective component, show dominant contributions to the improved SST bias in the tropics and midlatitudes. The difference in the convective flux between HR and LR CESM is partially attributable to the difference in the surface heat flux, and the other important contributing factor is the warmer subsurface temperature in HR CESM driven by the vertical eddy heat transport. Overall, this study highlights the importance of improving representation of ocean eddy and turbulent processes in climate models.

1 Introduction

Sea-surface temperature (SST) is a critical field to get right in simulations of the climate system because it is the key variable linking changes in the ocean to the atmosphere. SST anomalies associated with the El Niño-Southern Oscillation (ENSO), the Pacific Decadal Variability (PDV) and the Atlantic Multidecadal Variability (AMV) are all capable of modulating extreme weather globally (McPhaden et al., 2006; McCabe et al., 2004; Di Lorenzo and Mantua, 2016). The mesoscale SST anomalies in the northwestern Pacific can also influence heavy rainfall in western North America (Liu et al., 2021). To date, SST is also among the best measured climate fields, with long-term, global coverage obtained by ships (Woodruff et al., 2005; Smith et al., 2019), mooring buoys (TAO/TRITON, PIRATA, RAMA), Argo floats (Roemmich et al., 2009), and satellites (Reynolds and Smith, 1994).

Despite the fact that SST datasets are extremely useful for understanding global climate, it is still challenging to decipher the physical processes that govern SST, such as the relative roles of ocean mixing and advection, which are related to poorly-observed details of ocean circulation and eddy formation. Numerical models have therefore become extremely important tools to study SST mechanisms. SST bias, defined as the departure of simulated long-term mean SST from observations, is an important metric to assess model performance. The Coupled Model Intercomparison Project (CMIP), which began in 1995, provides a platform to compare simulated climate across different models (https://www.wcrp-climate.org/wgcm-cmip). The climate models participating in CMIP phase 5 (CMIP5), most of which have ocean and atmosphere horizontal resolutions of ~1°, show common biases in simulated climatological mean SST (Figure 1a). The biases can be divided into two groups: warm biases that primarily occur in the eastern boundary upwelling systems (EBUS), the Antarctic Circumpolar Current (ACC) region, and the east coasts of the U.S. and Japan;

and cold biases that occur mainly in the Tropics (also known as the cold tongue bias) and midlatitudes.

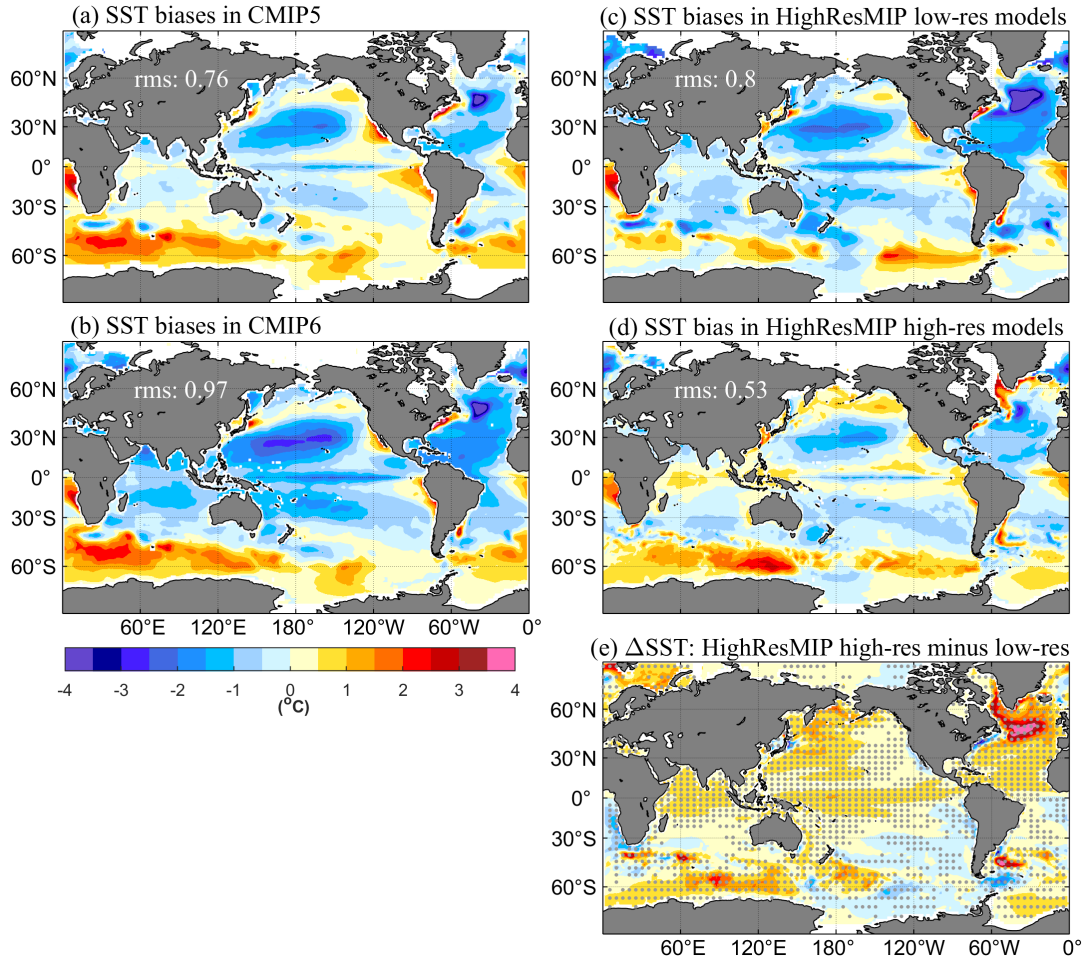

Figure 1. SST biases in (a) CMIP5 and (b) CMIP6, (c) HighResMIP low-resolution, and (d) high-resolution simulations. CMIP5 and CMIP6 biases are from the pre-industrial control simulations, usually 500 years long. For HighResMIP, 100-year-long 1950-control simulations are used. Climatological SST of HadISST1.0 (Rayner et al., 2003) for 1870-1880 and 1950-1960 is used in (a-b) and (c-d), respectively. (e) SST differences between HighResMIP high-resolution and low-resolution simulations (SST). HadGEM3-GC3.1, ECMWF-IFS, CNRM-CM6-1, EC-Earth3P, CESM1.3, and AWI-CM1.1in HighResMIP are used. Stippling in (e) indicates that at least 4 out of 6 HighResMIP models agree on the sign of SST. CMIP5 and CMIP6 models used here are listed in Table S2 and Table S3.

The impacts of SST bias on the simulated climate system have been extensively studied in recent decades (Large and Danabasoglu, 2006; Ashfaq et al., 2011; Camargo, 2013; He and Soden, 2016; McGregor et al., 2018; Lee et al.,2018; Hsu et al., 2019; Johnson et al., 2020; Dutheil et al., 2020; Garfinkel et al., 2020). These studies show that climatological SST biases can strongly affect global precipitation distributions, as well as future projections of precipitation over ocean and land (Ashfaq et al., 2011; He and Soden, 2016; Johnson et al., 2020). In addition, biases in tropical cyclone frequency, location, and intensity are strongly impacted by SST in the Tropics (Camargo, 2013; Hsu et al., 2019; Dutheil et al., 2020). Hsu et al. (2019) found that warm biases in the Pacific and cold biases in the Atlantic both can lead to overrepresentation of tropical cyclones in the Pacific. McGregor et al. (2018) also suggested that SST biases in the Atlantic basin can affect the wind and surface temperature in the Pacific via atmospheric teleconnections. Furthermore, the warm SST bias in the eastern tropical Pacific tends to cause a biased midlatitude stationary wave in the Southern Hemisphere through erroneous double Intertropical Convergence Zone (ITCZ) (Garfinkel et al., 2020). Lee et al. (2018) demonstrated that the SST bias in the Gulf Stream region can induce Rossby wave responses in the troposphere in the Northern Hemisphere. Moreover, Ying et al. (2019) showed that cold biases in the central equatorial Pacific can lead to La Niña-like warming patterns. Therefore, understanding the source of SST biases in models is vital for improving climate simulations and projections.

Gent et al. (2010) showed that warm biases in EBUS are significantly reduced after increasing the atmospheric resolution from 2° to 0.5° in the Community Climate System Model version 3.5 (CCSM3.5), pointing to the importance of atmospheric resolution in improving SST simulations in the upwelling regions. Xu et al. (2014) revealed that realistic coastal winds are important to reduce SST biases in the southeastern Atlantic. Based on three CCSM4 experiments with different atmospheric resolutions (0.5°, 1°, 2°), Small et al. (2015) showed that coastal wind stress curl is a dominant factor controlling SST biases via Sverdrup transport in EBUS, through its influence on poleward flow of warm tropical water. It was found that wind stress curl in 0.5° CCSM4 has a narrower coastal extent than in 1° and 2° CCSM4, leading to weaker poleward Sverdrup transport in 0.5° CCSM4 compared to 1° and 2° CCSM4 (Small et al., 2015). Kurian et al. (2021) demonstrated that improving the magnitude and spatial pattern of the Benguela coastal low-level jet plays a primary role in reducing SST biases in the Benguela upwelling region.

In contrast to the warm SST bias in EBUS, the source of cold SST biases in the tropics is still unclear. Song and Zhang (2009) found that SST biases are reduced after the convection schemes are modified in CCSM3, implying an important role for atmospheric convection processes. Li and Xie (2012) also argued that misrepresented cloud cover may be the main source of tropical SST biases in CMIP3 and CMIP5 models. Woelfle et al. (2018) presented evidence that the equatorial cold SST biases are directly generated by anomalous ocean advection driven by surface winds, which are sensitive to the underlying

convection parameterization in the Community Earth System Model version 1 (CESM1). On the other hand, Moum et al. (2013) proposed that vertical ocean mixing can also modulate SST biases in the equatorial Pacific. Moreover, Vannière et al. (2014) argued that the tropical cold SST biases are advected into the tropics from extratropics. Burls et al. (2017) further showed that it is the subtropical cell that brings cold SST biases to the tropics.

Studies of cold biases in the midlatitudes, especially western boundary regions, are more recent and still remain sparse. Kirtman et al. (2012) illustrated that CCSM3.5 generates warmer SST in the western boundary current regions and Southern Ocean after increasing ocean resolution from 1° to 0.1° with the same atmosphere resolution of 0.5°. Small et al. (2014a) performed high-resolution CESM simulations with atmosphere resolution of 0.25° and ocean resolution of 0.1° (hereafter HR), and found that SST biases in the western boundary currents are substantially reduced compared with low-resolution CESM with ocean and atmosphere resolution of 1° (hereafter LR). The reduced SST bias is mainly due to the finer ocean resolution (Small, pers. comm.). The ongoing High-Resolution Model intercomparison Project (HighResMIP, Haarsma et al, 2016) of CMIP6 is designed to shed further light on the impact of horizontal model resolution on climate simulations. Models participating in HighResMIP have ocean resolution finer than 0.25° and atmosphere resolution finer than 0.5°. Gutjahr et al. (2019) conducted a suite of experiments using the Max Planck Institute Earth System Model (MPI-ESM1.2) contribution to HighResMIP and showed that increasing atmosphere resolution tends to decrease SST almost globally while increasing ocean resolution tends to increase SST everywhere except in the upwelling regions. These results are consistent with previous studies using CCSM and CESM (Gent et al., 2010; Kirtman et al., 2012; Small et al., 2014a; Small et al., 2015) as well as the Hadley Centre Global Environment Model 3 – Global Coupled version 3.1 (HadGEM3-GC3.1; Roberts et al., 2019). However, the underlying mechanisms for midlatitude SST changes in HR models are still unclear, especially in eddy-active regions.

This study aims to investigate the impacts of model horizontal resolution on the representation of SST in the tropics and midlatitudes using a set of CESM simulations produced by the International Laboratory for High-resolution Earth System Prediction (iHESP), as well as seven other HighResMIP models. The CESM simulations follow the HighResMIP protocol (Haarsma et al., 2016) and represent CESM's contributions to HighResMIP. This manuscript is organized as follows. Models and methods are described in Section 2. SST biases in HR models are shown in Section 3. Section 4 presents a surface ocean heat budget analysis in HR and LR followed by an analysis of ocean mixing and advection in Section 5. Summary and discussion are given in Section 6.

2 Models and Methods

2.1 HighResMIP simulations

In HighResMIP, ocean and sea-ice component models are all at least 0.25°, and

atmosphere and land component models are all at least 0.5°. Among the eight participating models, there are six running at 0.25° in ocean and two running at 0.1° or finer (Table 1). Following the HighResMIP protocol, each of these models was used for two fully-coupled simulations: (i) spinup-1950 (hereafter, SPIN) – a short (30-50 years) simulation starting from January ocean temperature and salinity (EN4.0; Good et al., 2013) averaged over the period of 1950–1954, (ii) control-1950 (hereafter, CNTL) – a longer than 100-year continuation of SPIN with the same climate forcing corresponding to 1950 conditions (for details, refer to Figure 1 of Roberts et al., 2019). The following analysis will be mainly based on CNTL to investigate climatological SST biases.

HighResMIP models used in this study are: CMCC-CM2-(V)HR4 (Cherchi et al., 2019), ECMWF-IFS (Roberts et al., 2018), CNRM-CM6-1 (Voldoire et al., 2019), EC-Earth3P (Haarsma et al, 2020), HadGEM3-GC3.1 (Roberts et al., 2019), MPI-ESM1.2 (Gutjahr et al., 2019), CESM1.3 (Danabasoglu et al., 2012; Small et al., 2014a; Meehl et al., 2019), and AWI-CM1.1 (Semmler et al., 2017). Resolutions of each model are shown in Table 1. Six of the eight HighResMIP models (HadGEM3-GC3.1, ECMWF-IFS, CNRM-CM6-1, EC-Earth3P, CESM1.3, and AWI-CM1.1) have configurations with different oceanic resolutions, which can be used to assess the role of ocean resolution in improving SST biases.

Table 1. Models participating in HighResMIP. Resolution names are defined independently across models.

Model	HadGEM3-GC3.1	ECMWF-IFS	CNRM-CM6-1	EC-Earth3
Resolution names	LL, HM, HH	LR, HR	LR, HR	LR, HR
Atmosphere model	MetUM-HadGEM3-GA7.1	IFS cy43r1	ARPEGE 6.3	IFS cy36r4
Atmospheric horizontal resolution	2.5°, 0.5°, 0.5°	0.5°, 0.25°	2.5°, 1°	1°, 0.5°
Atmosphere levels	85	91	91	91
Ocean model	NEMO-HadGEM3-GO6.0	NEMO3.4	NEMO3.6	NEMO3.6
Oceanic horizontal resolution	1°, 0.25°, 1/12°	1°, 0.25°	1°, 0.25°	1°, 0.25°
Ocean levels	75	75	75	75

2.2 CESM

Given that we have access to full model output only from CESM but not from other models in HighResMIP, we will primarily analyze HR and LR CESM to address our scientific questions. In the following, we will particularly use HR and LR to refer to CESM simulations. CESM1.3 is an open source fully coupled climate model developed by the National Center for Atmospheric Research (NCAR). CESM1.3 is comprised of the Community Atmosphere Model version 5 (CAM5; Neale et al., 2012), the Parallel Ocean Program version 2 (POP2; Danabasoglu et al., 2012; Smith et al., 2010), the Community Land Model version 4 (CLM4; Lawrence et al., 2011) and the Community Ice Code version 4 (CICE4; Hunke and Lipscomb, 2008). As in Small et al. (2014a), HR has a nominal

resolution of 0.1° for POP2 and CICE4 and 0.25° for CAM5 and CLM4. In POP2, vertical mixing is represented by the K-Profile Parameterization (hereafter KPP; Large et al., 1994), which includes both local and nonlocal mixing components. For more detailed descriptions of CESM1.3, we refer the reader to earlier studies (Danabasoglu et al., 2012; Small et al., 2014a; Meehl et al., 2019; Chang et al., 2020).

LR is used for comparison with HR. LR has a nominal horizontal resolution of 1° for all component models, and the effects of mesoscale (10-100 km) and submesoscale (< 10 km) eddies are included using the Gent and McWilliams (1990; hereafter GM90) and the Fox-Kemper et al. (2008; hereafter FK08) parameterizations in POP2. Both GM90 and FK08 are turned off in HR, however the same KPP vertical mixing is used in both HR and LR.

The 54-year HR SPIN simulation included an initial tuning phase followed by several decades of integration, in accordance with the HighResMIP protocol. CNTL is a continuation of SPIN from year 55 to year 160 (hereafter CNTL-HR). For LR, only 30 years is used for SPIN, and CNTL is integrated from year 31 to year 181. To save on storage, only the first 20 years of SPIN output in HR (SPIN-HR) and LR (SPIN-LR) are saved. Since both SPIN-HR and SPIN-LR start from the same EN4.0 dataset, comparing SPIN-HR and SPIN-LR allows us to examine the development of SST differences between HR and LR.

Becasue 20-year output of SPIN-HR and SPIN-LR is short to study the development of the SST biases, we performed a parallel 106-year LR integration to compare directly with CNTL-HR. This simulation was initialized by ocean temperature and salinity fields obtained from the first day of CNTL-HR, and thus is referred to as CNTL-LR-HRIC. Note that CNTL-HR and CNTL-LR-HRIC have the same initial condition for temperature and salinity. Therefore, we can examine the development of SST differences by comparing CNTL-HR and CNTL-LR-HRIC.

2.3 Methods

CESM employs a free surface configuration with a variable-thickness surface layer. As shown in the Chapter 5.2.1 of Smith et al. (2010), the temperature equation of the model surface layer is expressed as

$$\frac{\partial}{\partial t}\left(1+\frac{\eta}{H}\right)T = -\frac{\partial uT}{\partial x} - \frac{\partial vT}{\partial y} + \frac{wT|_{-H}}{H} + \frac{Q_{\text{net}}-SW|_{-H}}{c_P\rho_0 H} + \kappa_H\left(\frac{\partial^2}{\partial x^2}+\frac{\partial^2}{\partial y^2}\right)T - \frac{\kappa_v}{H}\left(\frac{\partial T}{\partial z}-\gamma_x\right)|_{-H} + q_W T_W, \quad (1)$$

where is sea surface height (SSH); T is potential temperature; u, v, and w are velocity along x, y, and z axes, respectively; H=10 m; Q_{net} is the net surface heat flux including latent, sensible, longwave and shortwave heat flux at the surface, and the sign convention is that positive denotes heat flux into the ocean; $SW|_{-H}$ represents penetrative shortwave flux at z=-H; c_P is the ocean heat capacity taken as 3996 J/kg/°C; ρ_0 is the density of sea water taken as 1026 kg/m^3; $\kappa_H$and κ_v are spatially-varying horizontal and vertical diffusivity;

and γ_x represents nonlocal turbulent heat transport in KPP. As eddies are not resolved in LR, total heat transport (uT, vT, wT) is taken as the sum of resolved transport and parameterized transport by GM90 and FK08.

To obtain Eq.1, the following approximations are employed: (i) the advective and diffusive horizontal fluxes between $z = 0$ and $z =$ are set to zero; (ii) there is no advection of temperature across the surface with vertical velocity; (iii) the freshwater flux is able to advect temperature aross the surface ($q_W T_W$). We have confirmed closure of the Eq. 1 budget, where the SSH term is much smaller than heat flux and mixing terms (see Figure S1 and Supplemental). Therefore, it is reasonable to lump the SSH term together with mixing as the residual in the heat budget analyses if mixing is unvailable in the model output.

2.3.1 Spatial surface ocean heat budget

After integrating Eq.1 in time, the evolution of SST can be expressed as

$$T(t)-T(0) = \int_0^t \left(-\frac{\partial uT}{\partial x} - \frac{\partial vT}{\partial y} + \frac{wT|_{-H}}{H}\right) dt + \int_0^t \frac{Q_{\rm net}-SW|_{-H}}{c_P\,\mathrm{H}} dt + \int_0^t \kappa_H \left(\frac{\partial^2}{\partial x^2} + \frac{\partial^2}{\partial y^2}\right) T dt - \int_0^t \frac{\kappa_v}{H}\left(\frac{\partial T}{\partial z} - \gamma_x\right)|_{-H} dt - \left[\frac{\eta(t)}{H}T(t) - \frac{\eta(0)}{H}T(0)\right]. \quad (2)$$

Similar to Kurian et al. (2021), the equation of climatological mean SST can be obtained as

$$\frac{1}{t_0}\int_0^{t_0} T(t)dt - T(0) = \frac{1}{t_0}\int_0^{t_0}\int_0^t \left(-\frac{\partial uT}{\partial x} - \frac{\partial vT}{\partial y} + \frac{wT|_{-H}}{H}\right) + \kappa_H \left(\frac{\partial^2}{\partial x^2} + \frac{\partial^2}{\partial y^2}\right) T \mathrm{d}t dt + \frac{1}{t_0}\int_0^{t_0}\int_0^t \frac{Q_{\rm net}-SW|_{-H}}{c_P\,\mathrm{H}} \mathrm{d}t dt + \frac{1}{t_0}\int_0^{t_0}\int_0^t \frac{\kappa_v}{H}\left(\frac{\partial T}{\partial z} - \gamma_x\right)|_{-H} \mathrm{d}t dt - \frac{1}{t_0}\int_0^{t_0}\left[\frac{\eta(t)}{H}T(t) - \frac{\eta(0)}{H}T(0)\right] \mathrm{d}t, \quad (3)$$

where t_0 is the length of the period of interest. Because the long-term mean of horizontal mixing is generally quite small compared with other near-surface terms, it will be lumped with the advection term together. The balance in Eq.3 will be referred to as the spatial surface ocean heat budget. The first two terms on the right-hand side comprise the ocean heat transport convergence (OHTC) followed by the atmospheric flux convergence (AFC) and ocean vertical mixing flux convergence (VMFC), as well as the SSH effect. VMFC is not available from CNTL-HR output, but it is available from SPIN-HR. Therefore, VMFC, along with the SSH term, will be calculated as the residual in CNTL-HR. To gain a complete understanding of ocean mixing in HR and LR, SPIN-HR and SPIN-LR will be used to discuss VMFC in detail.

2.3.2 Globally averaged surface heat budget

After taking a global average of Eq.2, the globally averaged SST can be expressed as

$$\langle T(t)\rangle - \langle T(0)\rangle = \int_0^t \frac{\langle wT|_{-H}\rangle}{H} dt + \int_0^t \frac{\langle Q_{\rm net}\rangle - \langle SW|_{-H}\rangle}{c_P\,\mathrm{H}} dt - \int_0^t \left\langle \frac{\kappa_v}{H}\left(\frac{\partial T}{\partial z} - \gamma_x\right)|_{-H}\right\rangle dt - \left[\left\langle \frac{\eta(t)}{H}T(t)\right\rangle - \left\langle \frac{\eta(0)}{H}T(0)\right\rangle\right], \quad (4)$$

where angle bracket $< >$ represents a global average. The heat balance in Eq.4 is a function of time only because horizontal processes are eliminated by the

global average. Globally averaged SST is controlled by the globally averaged: (i) vertical heat transport (VHTC), (ii) AFC, (iii) VMFC, and (iv) SSH effect. Similar to the surface heat budget, the VMFC and SSH terms will be calculated as the residual due to their unavailability in CNTL-HR. Note that VMFC dominates the residual, which can be seen in the SPIN analyses in Section 4.

3 Mean SST in HighResMIP

Figure 1a and Figure 1b show SST biases in CMIP5 and CMIP6 piControl simulations, where observed SST is taken from HadISST1.0 averaged over 1870-1880. This analysis includes 28 CMIP5 models and 34 CMIP6 models, whose information is shown in Table.S1 and Table.S2, respectively. Most CMIP6 models have similar horizontal resolutions as their CMIP5 counterparts, around 1° in both atmosphere and ocean. It is evident that SST simulations show very little improvement from CMIP5 to CMIP6, and if anything a degradation, consistent with little change in model horizontal resolution.

Figure 1c shows the averaged SST biases from low-resolution versions of HadGEM3-GC3.1, ECMWF-IFS, CNRM-CM6-1, EC-Earth3P, CESM1.3 and AWI-CM1.1, where the first 100 years of CNTL are used. The observational benchmark used in Figure 1c is taken from HadISST1.0 averaged from 1950 to 1960, to match the 1950 forcing of the HighResMIP protocol. The results show similar bias patterns and magnitudes compared to the CMIP5 and CMIP6 piControl simulations, indicating that the climatological SST biases are not strongly sensitive to the choice of historical window.

Multi-model SST biases computed from 6 HighResMIP high-resolution simulations and the corresponding difference distributions between high-resolution and low-resolution simulations are shown in Figure 1d&e, respectively. It is evident that cold SST biases are reduced in most regions of the tropics and midlatitudes, but the bias turns from negative to positive in the high latitude North Pacific as well as near the equatorial Pacific and the equatorial Indian Ocean (Figure 1d), indicating overcorrections of SST biases in these regions. In addition, SST still shows warm biases in EBUS in high-resolution models (Figure 1d), even though the magnitude of the warm bias is significantly reduced in high-resolution models (Figure 1e), suggesting a positive impact of resolution increase on SST biases in all EBUS. As discussed in Small et al. (2015) and Kurian et al. (2021), the bias improvements in EBUS mainly result from improved representation of the alongshore wind structures due to atmospheric resolution increase. Additionally, there is a noticeable improvement of SST biases in eddy-active regions, including the Kuroshio extension (KE), Gulf Stream extension (GSE), Agulhas current, and Brazil current regions (Figure 1e). Finally, the warm SST biases in the SubAntarctic region becomes worse in high-resolution models (Figure 1d&e), which may be related to net surface flux changes, especially cloud-related shortwave fluxes (Hyder et al., 2018). Overall, the RMS of SST has decreased from 0.8 in HighResMIP low-resolution simulations to 0.53 in the corresponding high-resolution simulations.

The magnitudes of cold bias in low-resolution simulations can be more than 4°C in the North Atlantic (Figure 1a-c). As shown in Danabasoglu et al. (2010), SST in the North Atlantic is warmer in CCSM4 with Nordic Sea overflow parameterization than without overflow parameterization. Zhang et al. (2011) also pointed out that stronger Nordic Sea overflow can lead to warmer SST in the subpolar Atlantic, underscoring the importance of overflow representation for SST. Studies also showed positive correlation between SST bias in the North Atlantic and AMOC in CMIP5, implying smaller cold SST biases with stronger AMOC (Wang et al., 2014; Zhang and Zhao, 2015). In addition, the warm SST biases off the east coasts of the U.S and Japan, associated with incorrect paths of the Gulf Stream and Kuroshio currents, respectively, are largely improved in high-resolution models (Figure 1c and Figure 1d).

As presented in Figure S2, HighResMIP models still show large variations in SST improvements with resolution. All show improvements of SST in EBUS after increasing the atmosphere horizontal resolution, especially MPI-ESM1-2 and CMCC-CM2. By contrast, only four of the six models with different oceanic resolution configurations (CESM1.3, HadGEM3-GC3.1, ECMWF-IFS, and AWI-CM1.1) have warmer SST in the Tropics and western boundary regions of midlatitudes. In addition, the magnitude of SST difference between high-resolution and low-resolution simulations vary from model to model in the KE and GSE regions, ranging from about 0.5°C in ECMWF-IFS to 3°C in CESM1.3. Given the consistency of impacts of horizonal resolutions on SST in the Tropics and midlatitudes across CESM1.3, HadGEM3-GC3.1, ECMWF-IFS, and AWI-CM1.1, it is appropriate to use CESM1.3 to study SST changes from LR to HR in the Tropics and midlatitudes.

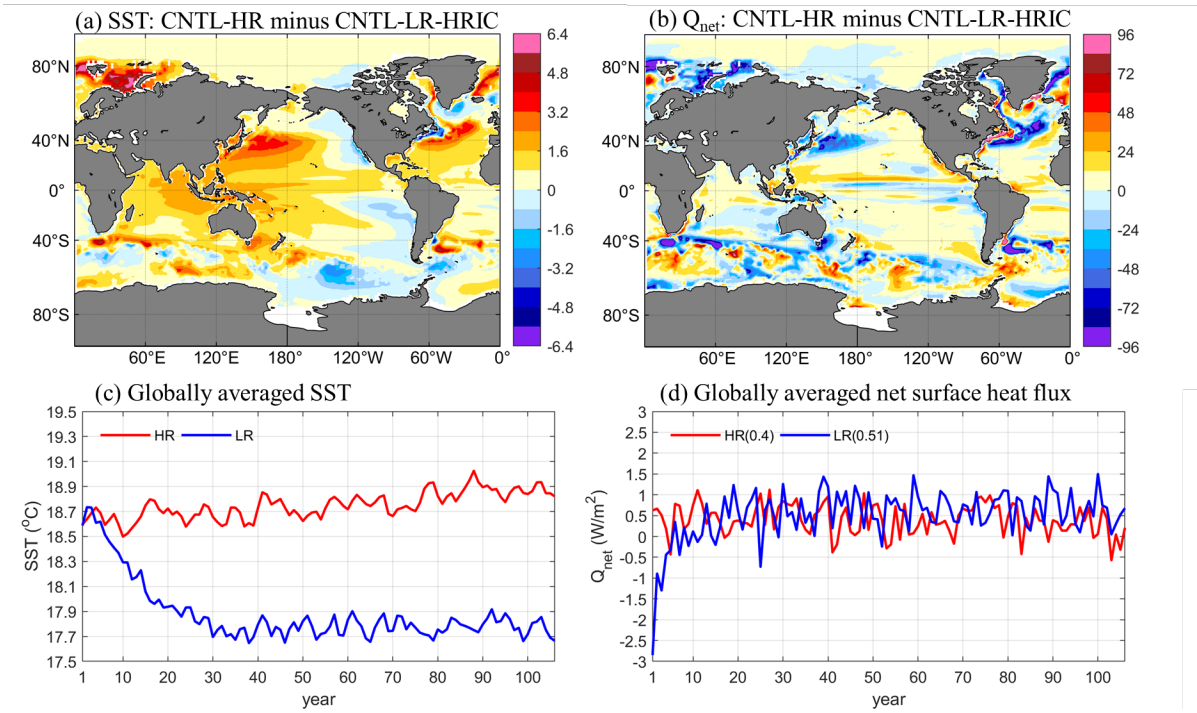

Figure 2. Differences of (a) SST and (b) Q_{net} between CNTL-HR and CNTL-LR-HRIC (106 years mean); globally averaged (c) SST and (d) Q_{net} in CNTL-HR (red) and CNTL-LR-HRIC (blue). Numbers in brackets in (d) are the time mean of Q_{net}. Units: °C in (a) and W/m^2 in (b).

Figure 2a shows SST difference between CNTL-HR and CNTL-LR-HRIC which is consistent with that shown in Figure S2. Globally averaged SST in CNTL-HR and CNTL-LR-HRIC are shown in Figure 2c. The global SST in CNTL-LR-HRIC (blue) is about 1°C cooler than CNTL-HR (red) after 30 years of integration. By the end of year 106, CNTL-LR-HRIC reaches a stable state with <SST> oscillating between 17.7 °C and 17.9 °C, while CNTL-HR still shows a warming trend of ~0.2 °C per century. As shown in Eq.2 and Eq.4, SST is determined by Q_{net} and other oceanic processes. The Q_{net} difference between CNTL-HR and CNTL-LR-HRIC is shown in Figure 2b. Note that there is more heat loss from the ocean in CNTL-HR in the eddy-active regions. This strongly suggests that the warmer SST in CNTL-HR is mainly associated with oceanic processes instead of Q_{net} in eddy-active regions. But Q_{net} can be a candidate to explain the warmer SST in the Tropics. The 106-year mean of globally averaged Q_{net} is about 0.4 W/m^2 in CNTL-HR and 0.51 W/m^2 in CNTL-LR-HRIC (Figure 2d), indicating that the warmer globally-averaged SST in CNTL-HR is due to oceanic processes.

SST and Q_{net} differences between SPIN-HR and SPIN-LR (Figure S3) are consis-

tent with those between CNTL-HR and CNTL-LR-HRIC in the tropics and midlatitudes (Figure 2a,b), indicating robust SST bias is already generated within 20 years of integration. However, the negative SST differences are larger and broader in the 20-year SPIN experiments in the subpolar Pacific and SubAntarctic regions, suggesting that the system is still under adjustment.

Note that the temperature difference between CNTL-HR and CNTL-LR-HRIC is larger at 45 m than the surface (Figure S4). Therefore, it is better to take SST as the temperature at the first level of model instead of the average over the upper 50 m or so to study SST differences. To investigate the details of the physical processes controlling SST in the tropics and midlatitudes, heat budget analysis described in Section 2.3 will be applied to HR and LR in the next section.

4 Heat balance in CNTL-HR and CNTL-LR-HRIC

4.1 Globally averaged surface heat budget

To diagnose the causes of the 1°C warmer <SST> in CNTL-HR than in CNTL-LR-HRIC (Figure 2c), globally averaged surface ocean heat budget analysis (Eq. 4) is conducted. As mentioned in Section 2, VMFC is calculated as the residual in CNTL-HR, as well as in CNTL-LR-HRIC for consistency. The residual should include both VMFC and SSH term, but be dominated by the former as discussed in Section 2.3. Therefere, the residual will be discussed as VMFC in the following. As shown in Figure 3a, the leading-order balance is between VMFC and AFC in CNTL-HR, with the latter broken down into non-shortwave heat flux AFC_tur (including sensible, latent, and longwave heat flux) and shortwave heat flux AFC_SW. Averaged over 106 years, AFC tends to cool down SST by 1916°C (1°C=4.10×10^6 J) while VMFC and VHTC tend to warm up SST by 1815°C and 101°C, respectively (Figure 3a). The decomposition of AFC indicates that AFC_tur tends to cool down SST by 7180°C, and this is partially compensated by AFC_SW with 5264°C warming. Furthermore, the cooling induced by AFC_tur is mainly attributable to the heat release by evaporation (See Figure S5). Since the amplitude of SST change is much smaller than other terms, it is plotted in Figure 3 with a scaling factor of 10 to visually check its sign.

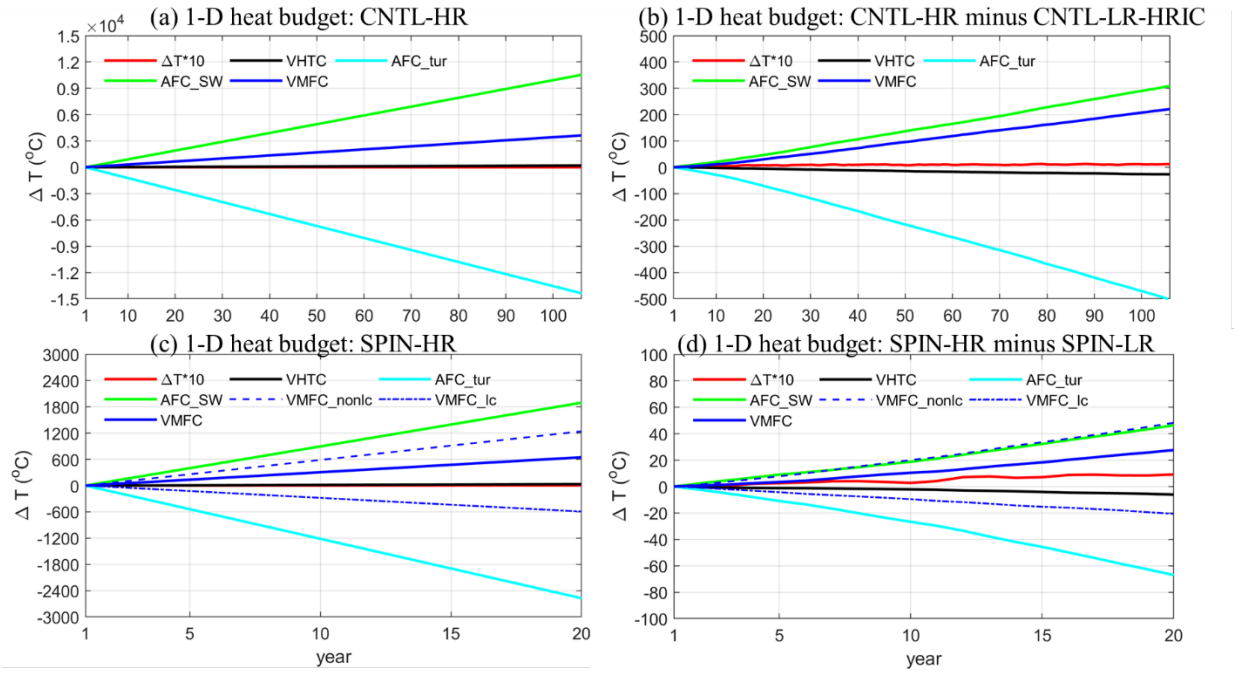

Figure 3. Heat budget of globally averaged SST in (a) CNTL-HR, (b) CNTL-HR minus CNTL-LR-HRIC, (c) SPIN-HR, and (d) SPIN-HR minus SPIN-LR. Red for SST changes, black for VHTC, cyan for AFC_tur, green for AFC_SW, solid blue for VMFC, dashed blue for VMFC_nonlc, and dot-dashed blue for VMFC_lc. Units are °C. VMFC in (a)(b) is obtained as the residual including SSH term, but not in (c)(d). SSH term is absent in (c)(d) because it is quite small.

Figure 3b shows the difference of each term in the globally averaged heat balance (Eq.4) between CNTL-HR and CNTL-LR-HRIC. Averaged over the 106 years, <SST> in CNTL-HR is 0.86°C warmer than CNTL-LR-HRIC. It is also clear that the warming effects of VMFC and AFC_SW are stronger in CNTL-HR than CNTL-LR-HRIC, generating 104.58°C and 148.31°C warmer SST in CNTL-HR, respectively. The differences in VMFC and AFC_SW account for 5.8% and 2.8% of the respective amplitude in CNTL-HR. In contrast, AFC_tur generates 237.36°C more cooling in CNTL-HR than CNTL-LR-HRIC, about 3.3% of that in CNTL-HR. The warming effect of VHTC is 14.68°C weaker in CNTL-HR than CNTL-LR-HRIC, showing a negative contribution to warmer <SST> in CNTL-HR. Therefore, VMFC is more important than other processes in generating warmer SST in CNTL-HR.

As shown in Large et al. (1994), VMFC parameterized by KPP includes local mixing (i.e., diffusive mixing, VMFC_lc) and nonlocal mixing (i.e., convective mixing, VMFC_nonlc). Diffusive mixing is proportional to the local vertical temperature gradient, while convective mixing is induced by convective insta-

bility within the boundary layer, which is nonzero only with unstable surface forcing. Therefore, the stronger warming induced by VMFC in HR is the net effect of the local and nonlocal mixing. To study the details of VMFC, the same globally averaged SST heat budget is also applied to the 20-year SPIN-HR and SPIN-LR (Figure 3c&d), in which the local and nonlocal KPP mixing terms were saved as model output. Solid lines in Figure 3c&d are exactly balanced and the two components of VMFC are represented by blue dashed lines. SPIN-HR and SPIN-LR essentially reproduce the results of CNTL-HR and CNTL-LR-HRIC, suggesting that we can use the shorter simulations from SPIN-HR and SPIN-LR to further decompose VMFC into VMFC_lc and VMFC_nonlc and investigate the detailed processes contributing to the SST difference between HR and LR.

Table 2. 20-year average of each term in the globally averaged heat budget of SPIN-HR and SPIN-LR (Unit: °C)

	SST	**VHTC**	**VMFC**	**AFC_SW**	**AFC_tur**	**SSH term**	
			Local	Nonlocal			
HR	0.32	17.31	-296.44	618.70	945.46	-1284.69	-0.02
LR	-0.18	20.05	-286.21	596.48	923.81	-1254.28	-0.03
HR-LR	0.50	-2.74	-10.23	22.22	21.65	-30.41	0.01

In SPIN-HR (Figure 3c), one can see that VMFC_nonlc tends to warm up SST, but VMFC_lc tends to cool down SST. Physically, VMFC_nonlc corresponds to convection when dense (cold) water is above lighter (warmer) water. Hence it tends to have a warming effect at the surface. VMFC_lc is primarily associated with diffusion of warm surface waters into the colder thermocline (hence a cooling effect). Compared with SPIN-LR, VMFC_nonlc and VMFC_lc are both stronger in SPIN-HR (Figure 3d). Table 2 shows the 20-year average of heat balance in SPIN-HR and SPIN-LR. SST in SPIN-HR is 0.5°C warmer than SPIN-LR, which is attributed to stronger VMFC_nonlc and AFC_SW. Contributions to the warmer SST from VMFC_nonlc and AFC_SW are 22.22°C and 21.65°C, respectively, which account for 3.6% and 2.3% of those in SPIN-HR. Therefore, VMFC_nonlc is slightly more important than AFC_SW in generating warmer SST in HR simulations from a global average perspective. Further details of why VMFC_nonlc differs between HR and LR will be discussed in Section 5.

4.2 Spatial surface ocean heat budget

Looking at spatial distributions of surface ocean heat budget contributors is useful to examine how the balance among various terms governing SST differences between HR and LR varies across geographic locations. Similar to the globally averaged heat budget, there are three main factors contributing to the evolution of the SST heat budget (Eq.3): OHTC, AFC and VMFC. OHTC here includes both vertical and horizontal advection processes. Each term in Eq.3 (with t_0

as 106 years) in CNTL-HR and CNTL-LR-HRIC are shown in Figure 4, where VMFC is calculated as the residual with the small SSH term included.

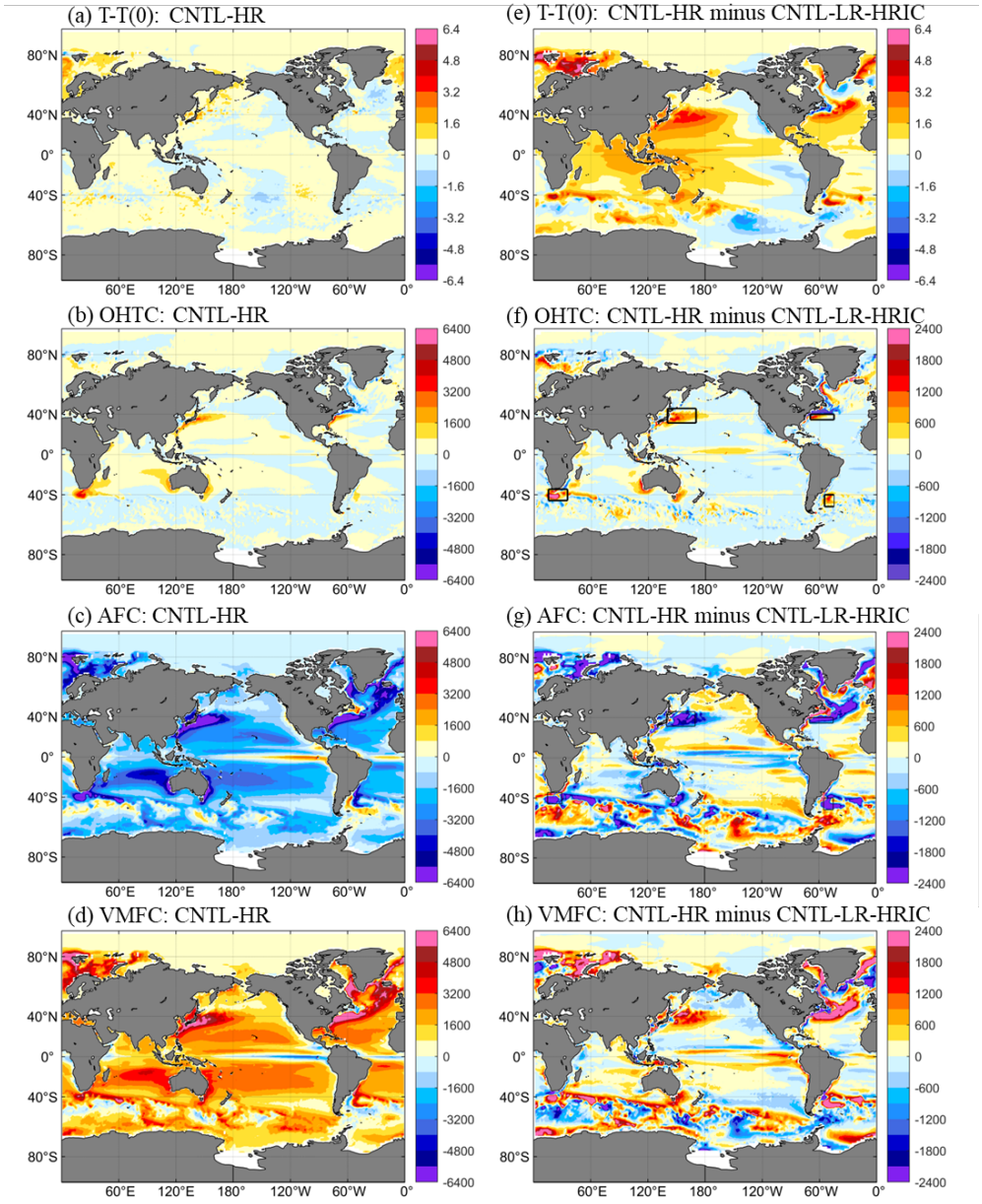

Figure 4. 106-year mean changes in CNTL-HR of (a) SST; (b) OHTC; (c) AFC; (d) VMFC. (e)-(h) similar to (a)-(d) but for CNTL-HR minus CNTL-LR-HRIC. Units are °C. The scale of (a) and (e) is smaller than other panels. Four boxes

in (f) indicates eddy-active regions with large OHTC differences.

As shown in Figure 4a, SST changes relative to the first year in CNTL-HR are small (less than 1°C) in 106 years. Consistent with the global-average heat budget (Figure 3a), the balance in spatial surface ocean heat budget is dominated by AFC (Figure 4c) and VMFC (Figure 4d) over most of the global ocean. Ocean advection, OHTC, only shows large contributions in eddy-active regions (Figure 4b). From Figure 4c, it is clear that heat loss within the upper 10 m of the ocean occurs everywhere, except in the equatorial regions, EBUS, and some SubAntarctic regions (Figure 4c). The heat loss indicates that the net shortwave heat flux within the upper 10 m is less than the outgoing non-shortwave heat fluxes. Due to the large compensation among OHTC, AFC, and VMFC, the scale of SST change is much smaller than the other three, similar to the global-average heat budget.

The differences between CNTL-HR and CNTL-LR-HRIC are demonstrated in Figure 4e-h. In much of the western and tropical basins, SST is warmer in CNTL-HR, especially in the eddy-active regions where the differences can reach 4°C (Figure 4e). The cooling induced by AFC is stronger in CNTL-HR in the eddy-active regions (Figure 4g), which is mainly contributed by the non-shortwave component AFC_tur (Figure 5b). On the other hand, AFC_SW is larger in CNTL-HR in the tropical and polar regions, but smaller in the EBUS and the Southern Ocean (Figure 5a), which is similar to the SST difference pattern in Figure 4e. The spatial correlation coefficient of SST difference (Figure 4e) and AFC_SW difference (Figure 5a) is 0.48, indicating that the shortwave heat flux and SST differences are closely related, but that other terms are involved. Like AFC_SW, OHTC also shows stronger warming in CNTL-HR in eddy-active regions (Figure 4f). VMFC differences (Figure 4h), which are the net effect of VMFC_lc and VMFC_nonlc, show a nearly opposite pattern from AFC, with the pattern correlation coefficient of -0.9.

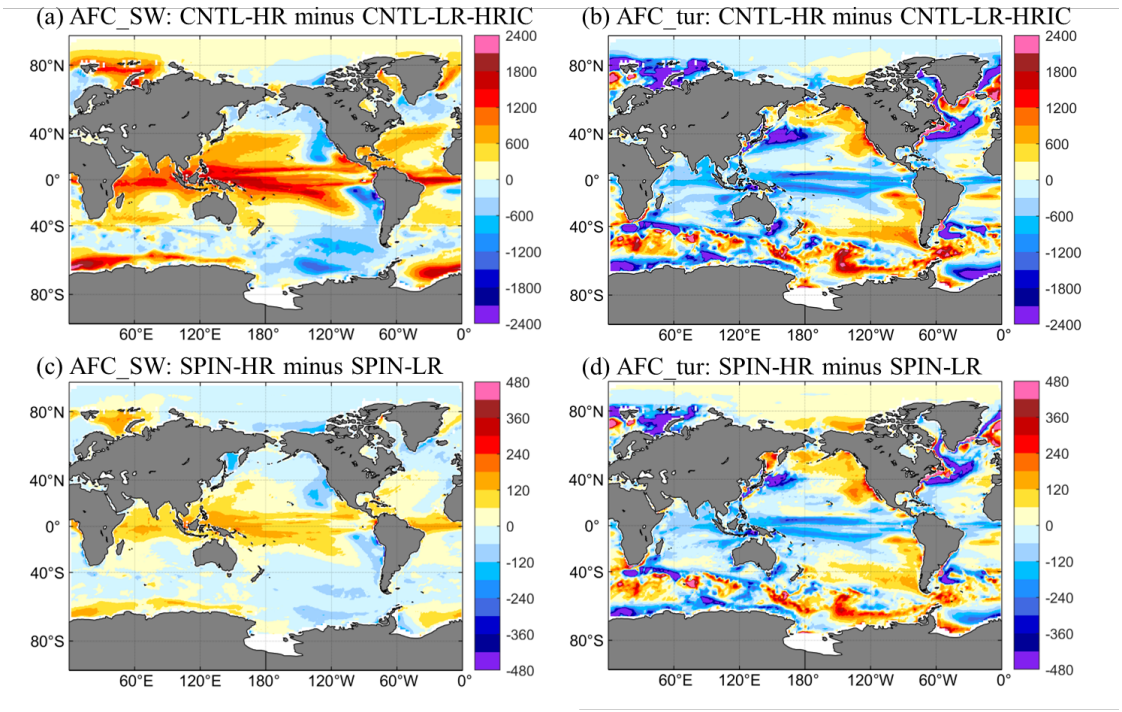

Figure 5. Difference of (a) AFC_SW and (b) AFC_tur between CNTL-HR and CNTL-LR-HRIC; (c) AFC_SW and (d) AFC_tur between SPIN-HR and SPIN-LR. Units: °C.

The relative importance of VMFC_lc versus VMFC_nonlc in the SST difference between HR and LR can be further investigated using direct model output from SPIN-HR and SPIN-LR. Figure S6 shows the results of a similar spatial surface ocean heat budget analysis using the 20-year simulations from SPIN-HR and SPIN-LR. Despite the shorter simulation length, the heat balance in SPIN-HR and SPIN-LR shows a very similar structure to that of CNTL-HR and CNTL-LR-HRIC. In both cases, OHTC and VMFC are primarily responsible for the warmer SST in HR in eddy-active regions (Figure S6, Figure 4), and AFC_SW and VMFC for the warmer SST in tropical regions (Figure 5c). As in the globally averaged heat budget, the short SPIN simulations can offer insight into the spatial surface ocean heat budget differences seen in the CNTL simulations.

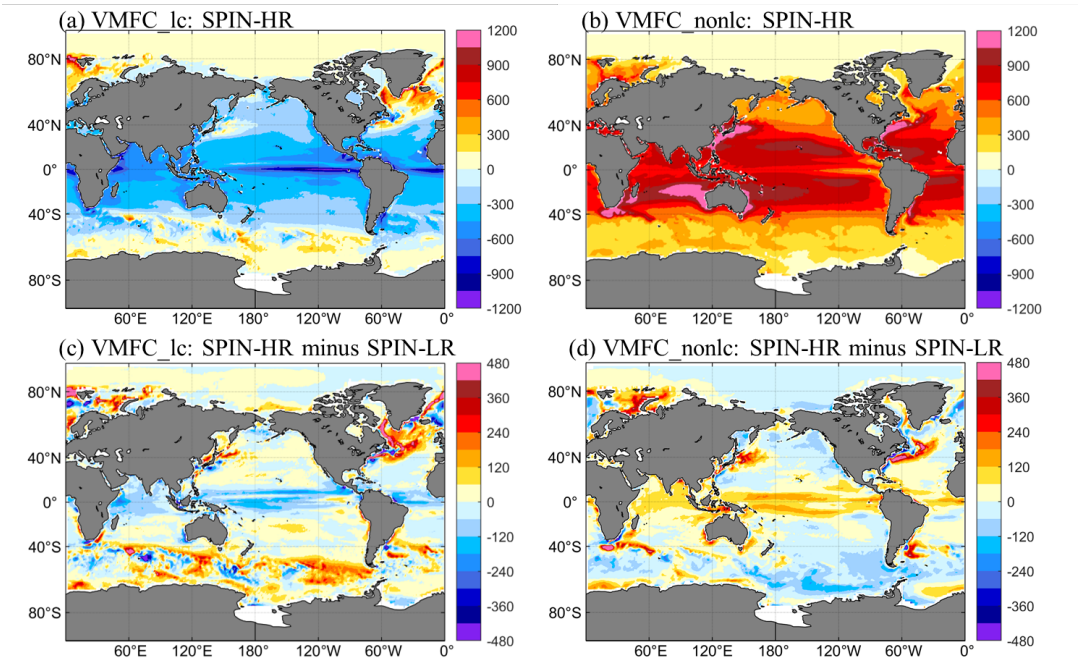

Figure 6. Breakdown of VMFC into (a) local and (b) nonlocal components in SPIN-HR. Difference of (c) VMFC_lc and (d) VMFC_nonlc between SPIN-HR and SPIN-LR. Units: °C.

In SPIN-HR, VMFC_lc tends to cool surface temperature except in high-latitude regions, and the strongest cooling occurs in equatorial regions (Figure 6a). In contrast, VMFC_nonlc tends to warm up the surface layer, with large amplitudes in eddy-active regions (Figure 6b). An examination of the differences of these two terms between SPIN-HR and SPIN-LR shows that VMFC_nonlc is stronger in SPIN-HR in eddy-active and tropical regions, while the difference of VMFC_lc shows generally opposite sign to that of VMFC_nonlc (Figure 6c&d).

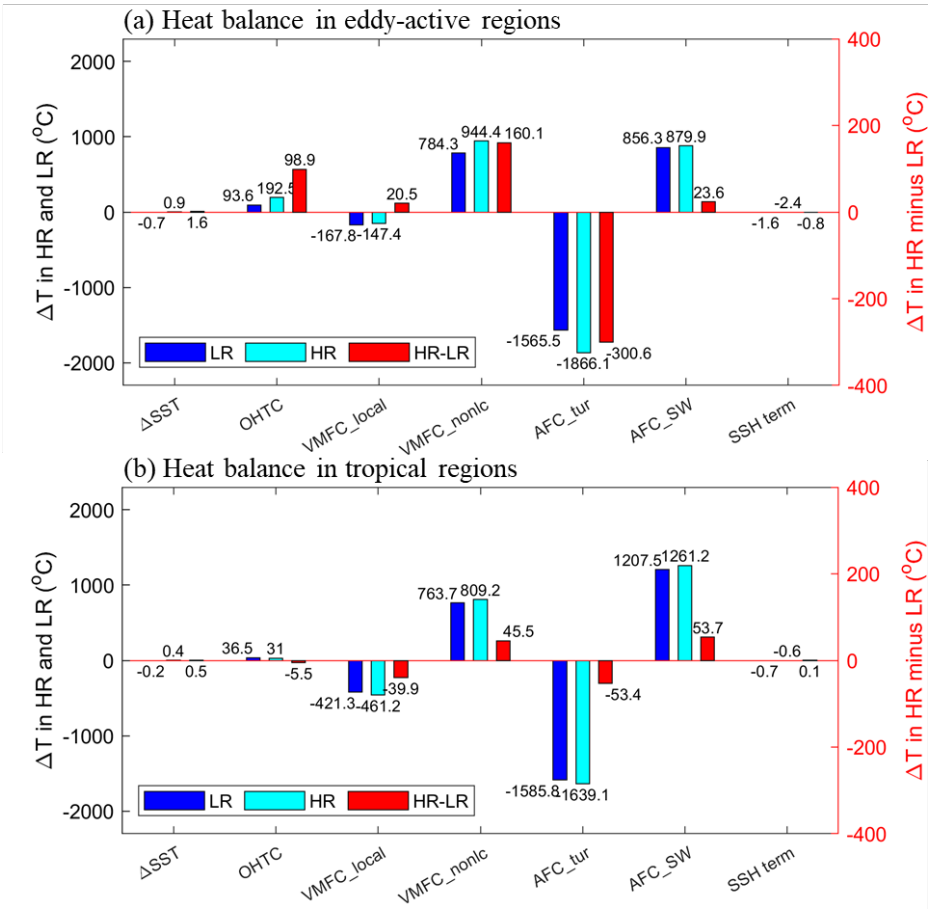

Figure 7. 20-year mean of heat balance (a) in 4 eddy-active regions labelled by black boxes in Figure 4f, and (b) tropical regions (30°S-30°N). Blue for SPIN-LR, cyan for SPIN-HR and red for SPIN-HR minus SPIN-LR.

Figure 7a shows 20-year mean of area-averaged heat balance in four eddy-active regions shown by boxes in Figure 4f. OHTC, VMFC_nonlc and AFC_SW all contribute positively to the heat budget of SPIN-HR (cyan) and SPIN-LR (blue), while VMFC_lc and AFC_tur contribute negatively. SST is about 1.6°C warmer in SPIN-HR than SPIN-LR in these eddy-active regions (red in Figure 7a), which is considerably larger than the globally averaged difference of 0.5°C. The stronger AFC_tur in SPIN-HR tends to cool down SST by 300.6°C, which is counterbalanced by the stronger OHTC (98.9°C), weaker local mixing (VMFC_lc, 20.5°C), stronger nonlocal mixing (VMFC_nonlc, 160.1°C) and stronger AFC_SW (23.6°C). Again, the SSH term contributes to the SST difference much less than other processes. Therefore, OHTC and VMFC_nonlc are the two most dominant factors in generating warmer SST in eddy-active regions, while AFC_SW plays a secondary role. This result also holds in each

eddy-active region as shown in Figure S7. Similar results from 106-year CNTL-HR and CNTL-LR-HRIC are shown in Figure S8a, confirming that vertical mixing and advection are the most important for warmer SST in the eddy-active regions in HR. Zhu et al. (2020) found that SST in the North Pacific will get warmer after increasing the strength of convective mixing in the LR ocean-only Modular Ocean Model version 5 (MOM5), which supports the finding that convective mixing is important to reduce the cold SST biases.

In the tropics (30°S-30°N), OHTC shows the smallest contribution to the heat budget in both SPIN-HR (cyan) and SPIN-LR (blue, Figure 7b). The SST in SPIN-HR is about 0.5°C warmer than SPIN-LR (red in Figure 7b), comparable to the global average of 0.5°C. Different from eddy-active regions, VMFC_lc is stronger in SPIN-HR than SPIN-LR in the tropics, generating cooler SST of 39.9°C, which is comparable with -53.4°C induced by stronger AFC_tur. In addition, VMFC_nonlc and AFC_SW are the only two processes contributing to warmer SST in SPIN-HR, producing 45.5°C and 53.7°C warming, respectively. They account for 5.6% and 4.3% of the corresponding value in SPIN-HR. Therefore, VMFC_nonlc is relatively more important than AFC_SW for the warmer SST in the tropics in HR. On the other hand, because there is strong compensation between VMFC_lc (-39.9°C) and VMFC_nonlc (45.5°C), the net warming effect of VMFC is only 5.6°C, which is much smaller than AFC_SW. This is consistent with CNTL-HR and CNTL-LR-HRIC results shown in Figure S8b.

As shown in Figure S9, there are fewer low clouds in regions where shortwave heat flux is larger in HR (Figure 5a&c), which may be related to impacts of model resolution on deep and shallow convection schemes in CAM5. We note that convection-related parameters in HR are kept the same as those in LR, which may be responsible for higher tropical precipitation in HR (Chang et al., 2020). Future exploration, which is beyond the scope of this work, is needed to investigate differences in parameterized clouds between HR and LR. In the next section, we will focus more on the causes of upper ocean vertical mixing and advection differences between SPIN-HR and SPIN-LR.

5 Vertical mixing and advection

5.1 Vertical mixing

5.1.1 Importance of shape function

As shown in Large et al. (1994) and Van Roekel et al. (2018), nonlocal KPP flux is parameterized as $\kappa_z \gamma_x = C_* \kappa \left(c_s \right)^{1/3} G(\sigma) \overline{(\mathrm{wT})}_{\mathrm{sfc}}$, where C_*, κ, c_s, and ε are constants defined in Large et al. (1994). In the following discussion, $C_* \kappa \left(c_s \right)^{1/3}$ is expressed as C for convenience. The nonlocal KPP flux is non-zero only in regions of unstable stratification caused by surface buoyancy flux. Under the assumption that heat flux dominates surface buoyancy flux, unstable conditions in CESM occur when the net heat flux absorbed in the boundary layer is negative, indicating a net heat loss from the surface. $\overline{(\mathrm{wT})}_{\mathrm{sfc}}$ is the

active surface kinematic fluxes, including the net longwave heat flux, sensible and latent heat flux (refer to Eq.A2c in Large et al., 1994; hereafter, referred to as Q_{ns}). In theory, shorwave radiation absorbed in the boundary layer (SWBL) can also contribute to the nonlocal KPP flux. Unfortunately, SWBL is not saved in SPIN-HR. However, Van Roekel et al. (2018) found that nonlocal KPP flux is not sensitive to SWBL. Therefore, the nonlocal KPP flux will be discussed in terms of Q_{ns} in the following, and can be simply rewritten as

$$\kappa_z \gamma_x = CG(\sigma) Q_{\mathrm{ns}} \ . \quad (5)$$

$G(\sigma)$ is the shape function expressed as a cubic polynomial

$$G(\sigma) = c_1 + c_2\sigma + c_3\sigma^2 + c_4\sigma^3, \quad (6)$$

where $\sigma = -\frac{z}{h},\ c_1 = 0,\ c_2 = 1,\ \ c_3 = -2 + 3G(1) - \left(\frac{\partial G}{\partial \sigma}\right)_{\sigma=1}, c_4 = 1 - 2G(1) + \left(\frac{\partial G}{\partial \sigma}\right)_{\sigma=1}$, h is the boundary layer thickness (HBLT) and σ varies from 0 to 1. The boundary conditions of the shape function at $\sigma = 1$ are determined by the mixing below the boundary layer (see details in Large et al. (1994) and Appendix B in Van Roekel et al. (2018)).

From Eq.5, the response of nonlocal KPP flux to surface heat forcing can be broken down into a direct response through Q_{ns} and an indirect response through the shape function $G(\sigma)$. To diagnose the differences of direct and indirect response between HR and LR, we can rewrite the the shape function and Q_{ns} in HR as $G_h = \Delta G + G_l$ and $Q_{\mathrm{nsh}} = \Delta Q_{\mathrm{ns}} + Q_{\mathrm{nsl}}$, where h and l represent HR and LR, respectively, and $\Delta(\bullet)$ denotes the difference between HR and LR. Therefore, the difference of nonlocal KPP flux between HR and LR can be expressed as

$$(\kappa_z\gamma_x)_h - (\kappa_z\gamma_x)_l = C\left[(\Delta G + G_l)\left(\Delta Q_{\mathrm{ns}} + Q_{\mathrm{nsl}}\right)\right] - CG_l Q_{\mathrm{nsl}} = C\left[\Delta G Q_{\mathrm{nsh}} + G_l \Delta Q_{\mathrm{ns}}\right]. \quad (7)$$

On the right side of Eq.7, the first term represents the impact of changes of shape function in HR from LR, which includes the negligible cross term (indirect response, hereafter VMFC_nonlcG), and the second term represents the impact of differences of non-shortwave heat flux (direct response, hereafter VMFC_nonlcQ).

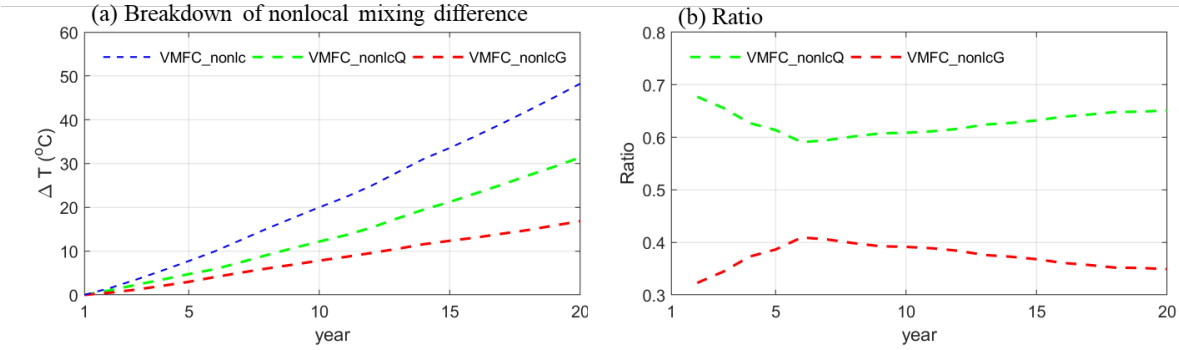

Figure 8. (a) Breakdown of VMFC_nonlc difference between SPIN-HR and SPIN-LR as shown in Figure 3d, blue dashed for VMFC_nonlc, green dashed for direct impact (VMFC_nonlcQ), red dashed for indirect impact (VMFC_nonlcG); (b) Ratio of VMFC_nonlcQ (green) and VMFC_nonlcG (red) divided by VMFC_nonlc difference between SPIN-HR and SPIN-LR. VMFC_nonlc is the summation of VMFC_nonlcQ and VMFC_nonlcG.

Figure 8a presents the breakdown of globally averaged VMFC_nonlc differences between SPIN-HR and SPIN-LR, clearly showing that VMFC_nonlcQ is larger than VMFC_nonlcG. The 20-year mean of VMFC_nonlcQ difference is 14.01°C, accounting for 63% of the total VMFC_nonlc difference. The ratio of VMFC_nonlcQ and VMFC_nonlcG over VMFC_nonlc are shown in Figure 8b with green and red dashed lines, respectively. The contribution of VMFC_nonlcQ to VMFC_nonlc is between 60-70%.

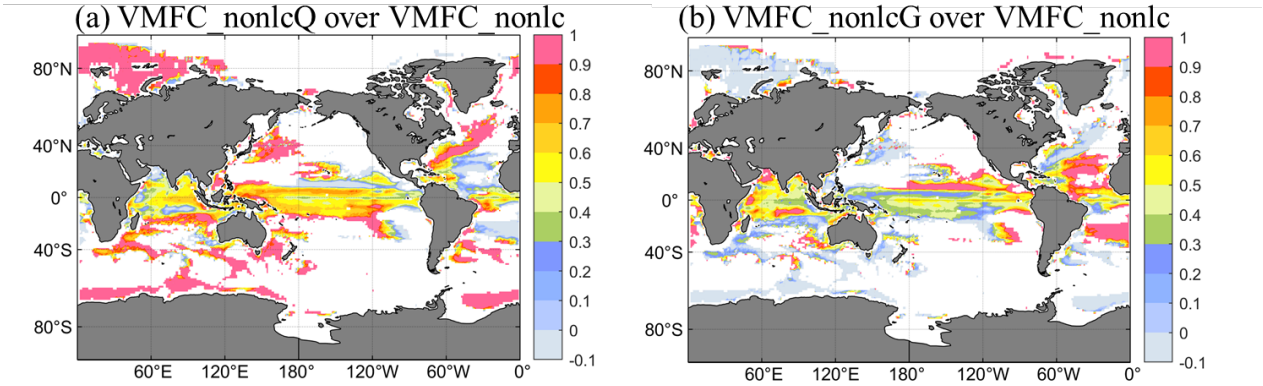

Figure 9. Ratio of (a) 20-year averaged VMFC_nonlcQ over 20-year averaged VMFC_nonlc and (b) 20-year averaged VMFC_nonlcG over 20-year averaged VMFC_nonlc for SPIN-HR minus SPIN-LR differences. Only regions where positive difference of VMFC_nonlc between SPIN-HR and SPIN-LR occurs (Figure 6d) are shown.

Figure 9a&b display spatial patterns of the ratios of VMFC_nonlcQ over VMFC_nonlc and VMFC_nonlcG over VMFC_nonlc, respectively, for SPIN-HR minus SPIN-LR difference. In the eddy-active regions, VMFC_nonlcQ can explain more than 90% of VMFC_nonlc differences. However, in the regions where the Gulf Stream separates from the U.S. coast, contributions of VMFC_nonlcQ and VMFC_nonlcG to VMFC_nonlc are similar (50%). In the tropics, VMFC_nonlcQ and VMFC_nonlcG both play an important role, accounting for 60% and 40% of VMFC_nonlc differences, respectively. These results reveal that VMFC_nonlcG cannot be neglected when we study the nonlocal KPP flux differences between HR and LR, indicating that oceanic processes are also important in modulating nonlocal KPP fluxes. In the following, we will investigate how the shape function can differ between HR

and LR.

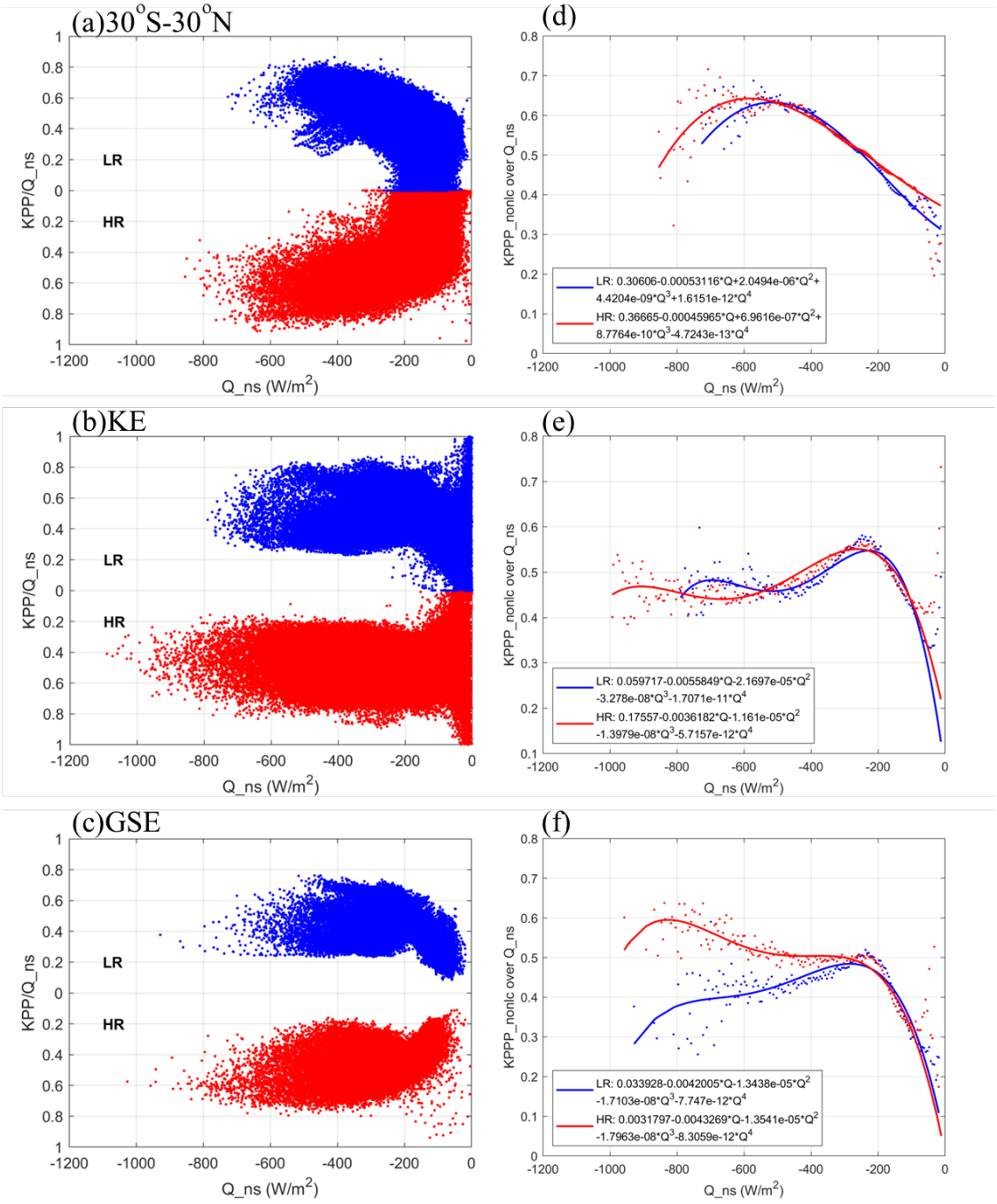

Figure 10. Shape function at 10 m as a function of Q_{ns} in (a) tropics, (b) KE,

and (c) GSE; heat flux-binned shape function in (d) tropics, (e) KE , and (f) GSE, each bin with width of 5 W/m^2. Dots for CESM results, solid lines for quartic fitting. Red for SPIN-HR and blue for SPIN-LR.

As shown in Eq.6, the shape function is modulated by the boundary layer thickness, which is defined as the shallowest depth where the bulk Richardson number Ri_b (refer to Eq.21 in Large et al., 1994) reaches 0.3. By definition, Ri_b can be influenced by the surface buoyancy forcing including freshwater and heat fluxes, indicating a nonlinear relationship between nonlocal KPP flux and surface heat flux. Figure 10a-c show the space- and time-varying shape functions at 10 m, which are estimated as the nonlocal KPP flux divided by the non-shortwave heat flux using monthly model output in the Tropics, KE, and GSE, respectively. It is clearly shown that the shape function varies strongly with respect to non-shortwave heat flux in both the tropics and eddy-active regions, confirming that nonlocal KPP flux is not a nonlinear function of nonsolar heat flux.

To mathematically quantify the nonlinearity, binned averages of the estimated shape function in the three regions are shown as dots with bin width of 5 W/m^2 in Figure 10d-f, and solid lines are the corresponding quartic fits to the data. The fitting coefficients are labelled in the legends in each panel. Results indicate that shape function is highly nonlinear in the large Q_{ns} regime (200 W/m^2) in both HR (red) and LR (blue). It is also shown that LR is less capable of simulating extremely strong Q_{ns} in the tropics (750 W/m^2) and KE (800 W/m^2). In these extreme Q_{ns} regimes, the shape function shows higher values in HR than LR, suggesting a larger contribution of VMFC_nonlcG. The possible oceanic processes that give rise to this nonlinearity will be discussed in the following section.

5.1.2 Role of eddies in nonlocal KPP mixing

The fitting polynomial shown in Figure 10 is a mathematical approximation of the relationship between the shape function and non-shortwave heat flux, and so it likely differs from the shape function computed in CESM. Nevertheless, this simple analysis shows that the shape function is a nonlinear function of non-shortwave heat flux, indicating that it is difficult to precisely decompose nonlocal KPP flux differences into contributions from the shape function and the surface heat flux. However, as shown in Eq.6, the shape function is modulated by HBLT, which is determined by the bulk Richardson number, indicating that oceanic processes can modulate the nonlinear relationship of shape function and Q_{ns} through local heat distributions. Vertical heat transport (VHT) in the ocean acts to redistribute heat, which impacts the bulk Richardson number. As shown in Wolfe et al. (2008), mean-flow induced vertical heat transport (MVHT) is downward and eddy-induced vertical heat transport (EVHT) is upward in the global average, a result also seen in other studies (Hieronymus and Nycander, 2013; Brierley et al., 2010; Griffies et al., 2015; von Storch et al., 2016; Su et al., 2018, 2020; Jing et al., 2020). To shed light on the influence of VHT on nonlocal KPP flux, we conducted sensitivity experiments by changing the strength of the submesoscale parameterization in LR CESM. In this param-

eterization, a parameter that controls the strength of submesoscale parameterization is the horizontal length scale (HLS) of the fronts (Fox-Kemper et al., 2011). Experiments with smaller HLS have stronger submesoscale eddy fluxes in the extratropics. The default value is 5 km (EXP5km), and we conducted two sensitivity experiments with HLS reduced to 3 km for 50 years (EXP3km) and 800 m (EXP800m) for 20 years. Both of these runs started from the first day of CNTL-LR and other model settings were kept the same.

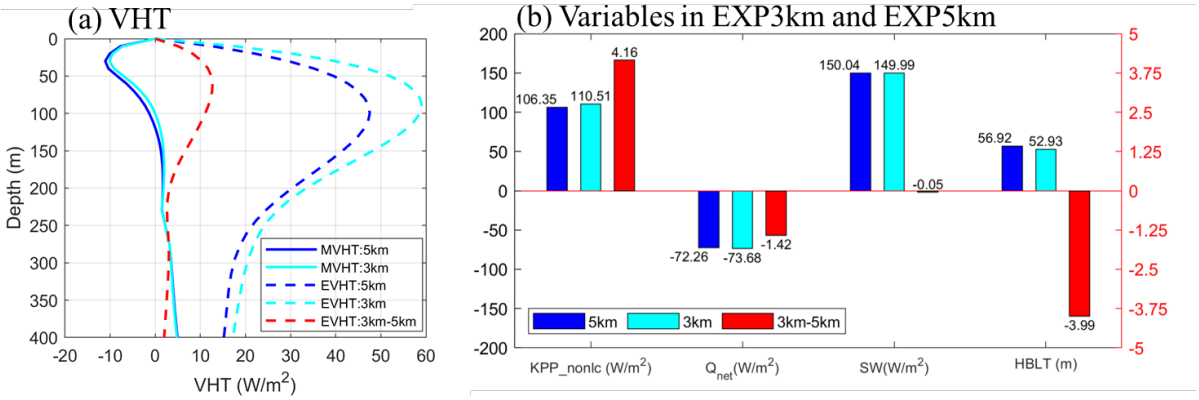

Figure 11. 50-year averaged (a) MVHT (solid) and EVHT (dashed) from EXP5km (blue), EXP3km (cyan), and EXP3km minus EXP5km (red); (b) nonlocal KPP flux, Q_{net}, SW at the surface, and HBLT from EXP5km (blue) and EXP3km (cyan) on the left y-axis, and EXP3km minus EXP5km (red) on the right y-axis. Results are combined over KE (145°E-170°E, 34°N-39°N) and GSE (65°W-50°W, 33°N-41°N). Units are shown in brackets following each variable.

The 50-year averaged results in EXP5km and EXP3km are shown in Figure 11. As demonstrated in Figure 11a, MVHT averaged over the combined KE (145°E-170°E, 34°N-39°N) and GSE (65°W-50°W, 33°N-41°N) region is slightly changed from EXP5km to EXP3km, but EVHT shows a significant increase with a maximum of 12.69 W/m^2 at 60 m (about 29.7% of EVHT in EXP5km). Figure 11b shows nonlocal KPP flux, Q_{net}, shortwave heat flux (SW), and HBLT in KE and GSE in EXP5km (blue) and EXP3km (cyan) on the left y-axis, as well as their difference (red) on the right y-axis. Nonlocal KPP flux is increased by 4% (4.16 W/m^2), and HBLT is decreased by 7% (3.99 m) from EXP5km to EXP3km. Similar results for 20-year mean in EXP5km, EXP3km, and EXP800m are shown in Figure S10. Nonlocal KPP flux (HBLT) keeps increasing (decreasing) from EXP5km, EXP3km to EXP800, indicating that the response of nonlocal KPP flux and HBLT to EVHT are monotonic. In contrast, Q_{net} is strengthened by about 2% (Figure 11b) or 3% (Figure S10b) from EXP5km to EXP3km, but it is weakened by 3.6% (Figure S10b) from EXP3km to EXP800m. In addition, SW shows little changes across three experiments. Therefore, the atmospheric response to submesoscale parameterization is weaker.

The EVHT and nonlocal KPP flux changes can be connected as follows. From Figure 11a, it is clear that there is a stronger VHT-induced local warming above 60 m and stronger VHT-induced local cooling below 60 m from EXP5km to EXP3km because the difference of EVHT reaches maximum at 60 m, indicating a more thermally stratified upper ocean in EXP3km. Therefore, HBLT is shallower in EXP3km than EXP5km. This result also holds at 20 years for these simulations as well as between EXP3km and EXP800m shown in Figure S10a. As a consequence, the stronger warming between 10 m and 60 m in EXP3km and EXP800m can provide more heat to the top 10 m for nonlocal KPP mixing.

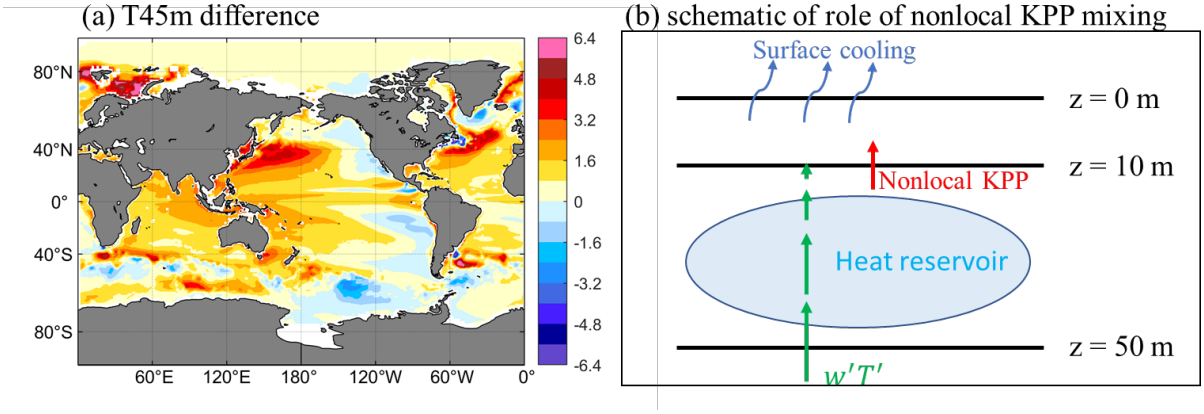

Figure 12. (a) T45m (°C) difference between CNTL-HR and CNTL-LR-HRIC; (b) schematic of role of nonlocal KPP mixing in modulating SST.

Although HBLT is not saved in the output in CNTL-HR and CNTL-LR-HRIC, we can check the difference in temperature at 45 m (T45m) between CNTL-HR and CNTL-LR-HRIC as shown in Figure 12a. It is clear that the T45m is warmer in CNTL-HR than CNTL-LR-HRIC in most regions, especially in eddy-active regions (also true in SPIN-HR and SPIN-LR, Figure S11), indicating there is more heat for nonlocal KPP mixing to move into the upper 10 m in HR than LR. In line with the finding in Jing et al. (2020), we propose the mechanism of nonlocal KPP mixing modulating SST as follows. As shown in Figure 12b, the surface heat loss will lead to strong eddy vertical heat transport ($w^{'}T^{'}$) based on the theory in Jing et al. (2020). Since $w^{'}T^{'}$ peaks around 50 m (Jing et al., 2020) and decreases to zero at the sea surface, the heat convergence by $w^{'}T^{'}$ is greatest between 10 m and 50 m, which can be regarded as a heat reservoir for the upper 10 m. Based on Figure 4g and Figure 12b, the cooling at the surface and the warming below 10 m are both stronger in HR than LR, which feeds a stronger nonlocal KPP flux, bringing more heat to the upper 10 m. Although nonlocal KPP flux is parametrized in CESM, the determination of HBLT is essentially a reflection of this physical process.

5.2 Ocean advection

As shown in Figure 7a, OHTC, including horizontal and vertical components, is the second largest factor in generating warmer SST in HR in eddy-active regions, corresponding to 62% of the contribution from VMFC_nonlc. OHTC is further decomposed into mean-flow-induced OHTC (MOHTC) and eddy-induced OHTC (EOHTC), where eddies are defined as the deviation from the monthly mean in HR and as parameterized eddies in LR. Since KE and GSE are the two largest eddy-active regions, analysis in this section will be mainly focused on KE and GSE.

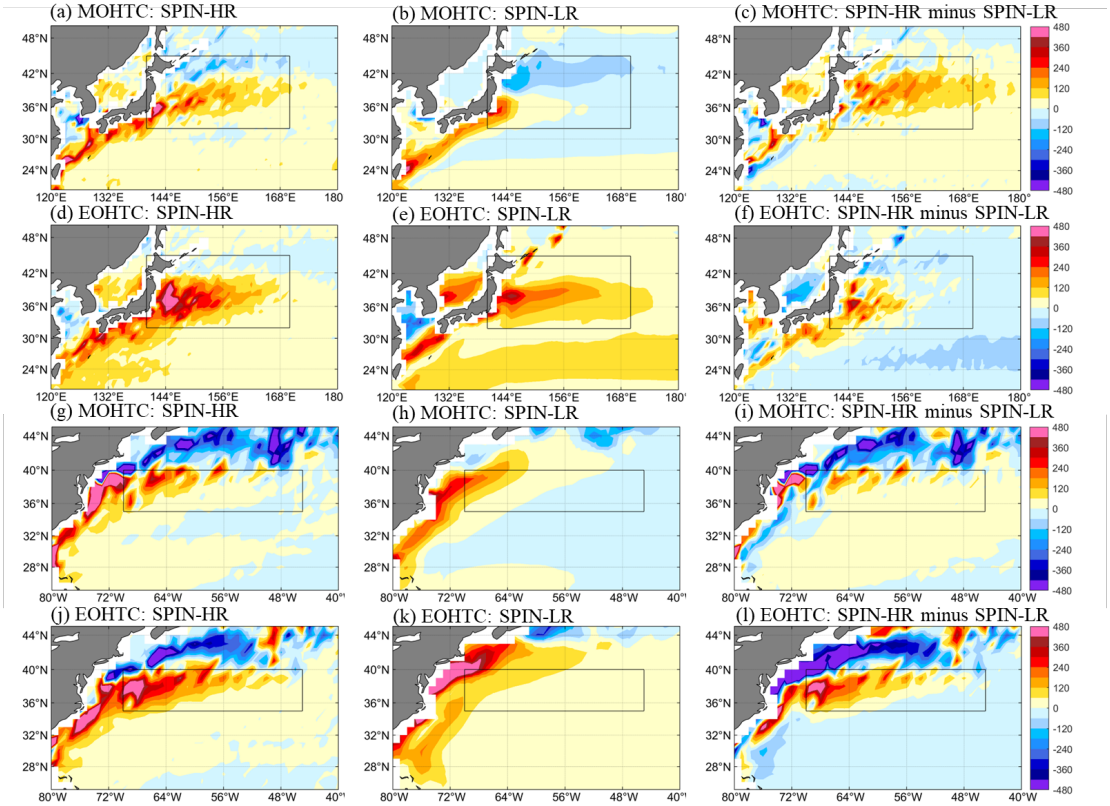

Figure 13. (a) MOHTC in SPIN-HR (b) MOHTC in SPIN-LR, (c) MOHTC difference between SPIN-HR and SPIN-LR, (d) EOHTC in SPIN-HR, (e) EOHTC in SPIN-LR, (f) EOHTC difference between SPIN-HR and SPIN-LR in KE. (g)-(l) are the same as in (a)-(f) but for GSE. Units for MOHTC and EOHTC: °C.

Differences of MOHTC and EOHTC between SPIN-HR and SPIN-LR in KE and GSE are shown in Figure 13. As in Figure 4, the boxes delineate regions where OHTC in HR and LR show large differences. In KE, the warming induced by MOHTC extends more northward and eastward compared with LR (Figure 13a&b), leading to warmer MOHTC-related SST difference between HR and

LR in the boxed region (Figure 13c). In contrast, EOHTC in HR and LR shares a similar spatial pattern in KE (Figure 13d&e), but produces a stronger warming in HR in the region where the Kuroshio current separates from Japan (Figure 13f). In the boxed region, MOHTC tends to generate 69.51°C warmer SST in SPIN-HR than SPIN-LR, which is more than 8 times larger than the contribution from EOHTC (8.42°C).

In GSE, MOHTC and EOHTC in LR both reflect a more severe overshoot of the Gulf Stream (Figure 13j&k) compared with HR (Figure 13g&h) (see also Small et al., 2014a). The improved Gulf Stream in HR explains the dipole pattern in the differences of MOHTC and EOHTC between HR and LR (Figure 13i&l). In contrast to KE, MOHTC in the GSE box only contributes to warmer SST by 32.75°C (Figure 13i), which is smaller than the contribution from EOHTC (58.27°C, Figure 13l).

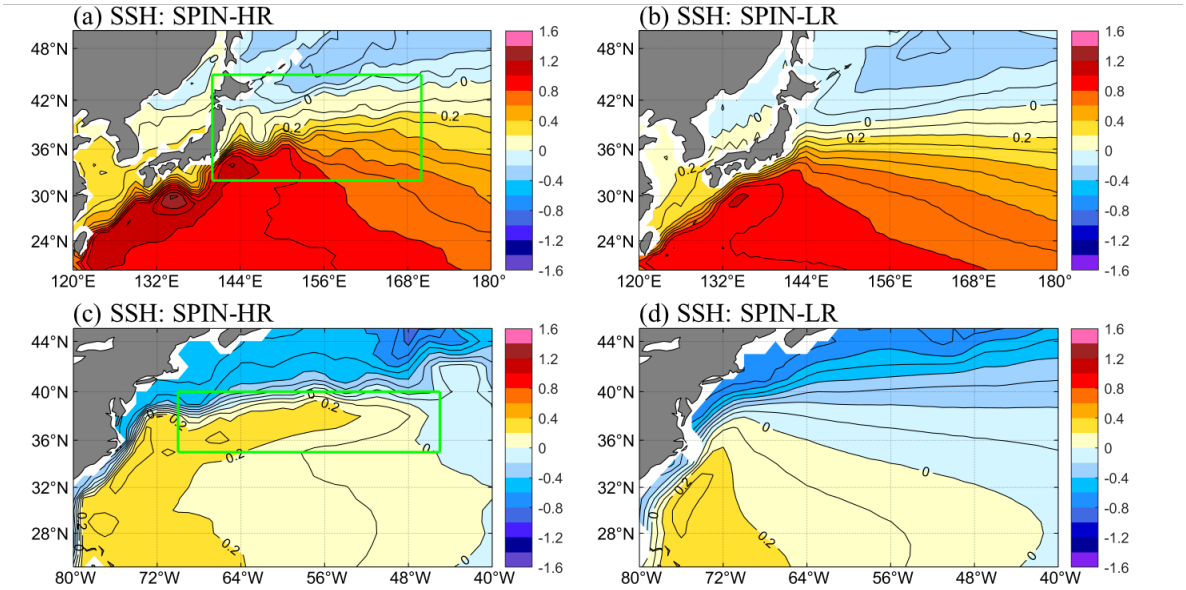

Figure 14. SSH in (a) and (b) KE and in (c) and (d) GSE from SPIN-HR and SPIN-LR. Units: m.

To investigate in more detail the mean circulation in KE and GSE, SSH is shown in Figure 14. In KE, the boundary between the subpolar and subtropical gyres is along 42°N in SPIN-HR, which is to the north of that in SPIN-LR (zero lines in Figure 14a&b). In addition, the strength of currents offshore of Japan is greater in SPIN-HR than SPIN-LR, as is the strength of recirculation flow. These differences lead to more warm water advected into the boxed region in SPIN-HR than SPIN-LR. In GSE, the recirculation in SPIN-HR is stronger and extends further eastward than in SPIN-LR. The overshoot problem is improved in SPIN-HR, which is consistent with the advection patterns in Figure 13j&k.

The improvement of the Gulf Stream in POP2 simulations has also been noted by Bryan et al (2007) by increasing horizontal resolution to 0.1°. They showed that the separation of the GS is sensitive to dissipation parameter choices. As summarized in Chassignet and Marshall (2008), there are many other factors that can influence the GS separation, for instance, subpolar gyre strength, Deep western boundary current, and representation of topography.

6 Summary and discussion

6.1 Summary

A recent study by Ma et al. (2021) showed that CMIP6 models share the same SST biases as previous CMIP5 models. Given that these two generations of climate models have similar horizontal resolution of ~1°, it raises the question of how SST biases are related to model resolution in these climate models. The present study attempts to address this question by analyzing the HighResMIP multi-model ensemble, which is a new model intercomparison project endorsed by CMIP6, aimed at assessing the impacts of climate model horizontal resolution on climate simulations. We particularly focus on examination of a set of HighResMIP simulations conducted by iHESP using CESM1.3, which includes a pair of 106-year high- and low-resolution control simulations (CNTL-HR and CNTL-LR-HRIC), and another pair of 20-year high- and low-resolution spin-up simulations (SPIN-HR and SPIN-LR). In each pair, the simulations have the same temperature and salinity initial conditions, so that initial state differences will not have an impact on ocean heat budget analysis. Seven other eddy-resolving and eddy-permitting models in the HighResMIP ensemble, including HadGEM3-GC3.1, AWI-CM-1-1, and ECMWF-IFS, are also analyzed and compared to CESM1.3. The results confirm that increasing model resolution can substantially reduce SST biases, including the warm bias in EBUS and cold bias in the western basins and tropics. The focus of this study is on the cold bias as it has not been thoroughly investigated by previous studies.

To investigate SST bias differences between HR and LR, both globally averaged and spatial surface ocean heat budget analyses are applied to the simulations. The globally averaged heat budget analysis reveals that the heat balance in the uppermost 10 m is mainly between atmospheric fluxes (i.e., AFC) and oceanic vertical mixing (i.e., VMFC) in both HR and LR, while vertical advection (i.e., VHTC) plays a secondary role. At the surface, non-shortwave heat flux cools the ocean. The solar radiation absorbed in the top 10 m cannot completely compensate the cooling induced by non-shortwave heat flux. Therefore, vertical mixing is important to close the budget by generating warming in the upper 10 m. Further decomposition indicates that it is the convective heat flux that accounts for the warming in the top 10 m through nonlocal vertical mixing from the subsurface to the uppermost layer. The differences of heat budget terms between HR and LR suggest that it is shortwave heat flux and nonlocal vertical mixing that account for the 1°C warmer global SST in HR.

Spatial surface ocean heat budget analysis demonstrates that stronger

VMFC_nonlc and AFC_SW in HR are mainly located in the eddy-active regions and the tropics, but the dominant term differs between eddy-active regions and the tropics. In the eddy-active regions, VMFC_nonlc (160.1°C) contributes the most to warmer SST in HR, followed by OHTC (98.9°C) and AFC_SW (23.6°C), and the importance of the latter is different from the globally averaged results. Further analysis shows that the stronger VMFC_nonlc in eddy-active regions in HR is mainly induced by the direct impact of non-shortwave heat flux instead of indirect impact via changes in the shape function. Regarding OHTC, it is found that the improvements in the strengths and positions of the western boundary currents favor warmer SST in HR, especially in KE and GSE. In the tropics, VMFC_nonlc and AFC_SW both contribute to warmer SST in HR by 45.5°C and 53.7°C, respectively, consistent with the globally averaged results. The stronger AFC_SW is likely induced by fewer clouds in HR, which may be related to model resolution impacts on cloud parameterizations. In contrast to eddy-active regions, both the direct and indirect impact of non-shortwave heat flux on nonlocal KPP flux contribute to the warmer SST in HR, accounting for 60% and 40%, respectively, of the nonlocal VMFC difference between HR and LR. It is also confirmed that the shape function responds to surface heat flux forcing in a nonlinear manner in both eddy-active regions and tropics, indicating that oceanic processes can strongly modulate the shape function. Based on three submesoscale parameterization sensitivity experiments, we proposed that the eddy induced vertical heat transport below 10 m can modulate nonclocal KPP mixing in the top 10 m.

6.2 Discussion

Although HadGEM3-GC3.1, AWI-CM-1.1, and ECMWF-IFS show SST differences between high-resolution and low-resolution simulations that are consistent with CESM, only AWI-CM-1.1 employs the same vertical mixing parameterization as in CESM while the other two use a turbulent kinetic energy (TKE) parameterization. In the TKE scheme, turbulent tracer flux is nonzero only with nonzero vertical gradient of mean quantities, which is not determined by the surface buoyancy forcing at all (Pandey and Dwivedi, 2021). Therefore, more analysis should be conducted to confirm the impact of vertical mixing on the SST difference between high-resolution and low-resolution HadGEM3-GC3.1 and ECMWF-IFS.

The dominant component of non-shortwave heat flux difference between LR and HR is the latent heat flux, especially in the midlatitudes. Wu et al. (2019) showed that the latent heat flux becomes stronger in the midlatitudes as they increase the atmosphere resolution from 130 km, 60 km to 25 km using the atmosphere component of Met Office's Unified Model. Minobe et al. (2008) pointed out that sharp SST gradients are vital to generate surface wind convergence which induces a stronger latent heat flux. Small et al. (2014b) also confirmed that SST fronts can modulate turbulent heat fluxes through changes of the surface stability using CAM4. Although previous studies were based on

atmosphere only experiments, they provide hints that differences of turbulent heat fluxes between LR and HR are highly associated with SST fronts in the midlatitudes, which needs more analyses in future work.

Acknowledgments

This research uses simulations performed by the International Laboratory for High Resolution Earth System Prediction (iHESP)—a collaboration among the Qingdao National Laboratory for Marine Science and Technology (QNLM), Texas A&M University (TAMU), and the U.S. National Center for Atmospheric Research (NCAR). This research is partially supported by NSF grant#2137684. NCAR is a major facility sponsored by the US NSF under Cooperative Agreement 1852977. G. Xu acknowledges the support from the China Scholarship Council. Authors thank Texas A&M University Supercomputing Facility. Special thanks go to Frederic Castruccio and Nan Rosenbloom for assistant in running the CESM simulations.

Open Research

CNTL-HR is available at https://ihesp.github.io/archive/products/ds_archive/Datasets.html#global-datasets. CNTL-LR-HRIC, SPIN-HR and SPIN-LR are available on the High-Performance Computer 'Grace' at Texas A&M University. Analyses are conducted using NCL and Matlab on Grace.

References

Ashfaq, M., Skinner, C. B., & Diffenbaugh, N. S. (2011). Influence of SST biases on future climate change projections. *Climate Dynamics*, 36(7-8), 1303-1319. https://doi.org/10.1007/s00382-010-0875-2

Brierley, C. M., Collins, M., & Thorpe, A. J. (2010). The impact of perturbations to ocean-model parameters on climate and climate change in a coupled model. *Climate Dynamics*, *34*(2), 325-343. https://doi.org/10.1007/s00382-008-0486-3

Bryan, F. O., Hecht, M. W., & Smith, R. D. (2007). Resolution convergence and sensitivity studies with North Atlantic circulation models. Part I: The western boundary current system. *Ocean Modelling*, *16*(3-4), 141-159. https://doi.org/10.1016/j.ocemod.2006.08.005

Burls, N. J., Muir, L., Vincent, E. M., & Fedorov, A. (2017). Extra-tropical origin of equatorial Pacific cold bias in climate models with links to cloud albedo. *Climate Dynamics*, *49*(5), 2093-2113. https://doi.org/10.1007/s00382-016-3435-6

Camargo, S. J. (2013). Global and regional aspects of tropical cyclone activity in the CMIP5 models. *Journal of Climate*, 26(24), 9880-9902. https://doi.org/10.1175/JCLI-D-12-00549.1

Chang, P., Zhang, S., Danabasoglu, G., Yeager, S. G., Fu, H., Wang, H., ... & Wu, L. (2020). An unprecedented set of high-resolution earth system

simulations for understanding multiscale interactions in climate variability and change. *Journal of Advances in Modeling Earth Systems*, *12*(12), e2020MS002298. https://doi.org/10.1029/2020MS002298

Chassignet, E. P., & Marshall, D. P. (2008). Gulf Stream separation in numerical ocean models. *Geophysical Monograph Series*, *177*. https://doi.org/10.1029/177GM05

Cherchi, A., Fogli, P. G., Lovato, T., Peano, D., Iovino, D., Gualdi, S., ... & Navarra, A. (2019). Global mean climate and main patterns of variability in the CMCC-CM2 coupled model. *Journal of Advances in Modeling Earth Systems*, *11*(1), 185-209. https://doi.org/10.1029/2018MS001369

Danabasoglu, G., Bates, S. C., Briegleb, B. P., Jayne, S. R., Jochum, M., Large, W. G., ... & Yeager, S. G. (2012). The CCSM4 ocean component. *Journal of Climate*, *25*(5), 1361-1389. https://doi.org/10.1175/JCLI-D-11-00091.1

Danabasoglu, G., Large, W. G., & Briegleb, B. P. (2010). Climate impacts of parameterized Nordic Sea overflows. *Journal of Geophysical Research: Oceans*, 115(C11). https://doi.org/10.1029/2010JC006243

Di Lorenzo, E., & Mantua, N. (2016). Multi-year persistence of the 2014/15 North Pacific marine heatwave. *Nature Climate Change*, *6*(11), 1042-1047. https://doi.org/10.1038/nclimate3082

Dutheil, C., Lengaigne, M., Bador, M., Vialard, J., Lefèvre, J., Jourdain, N. C., ... & Menkès, C. (2020). Impact of projected sea surface temperature biases on tropical cyclones projections in the South Pacific. *Scientific Reports*, 10(1), 1-12. https://doi.org/10.1038/s41598-020-61570-6

Fox-Kemper, B., Danabasoglu, G., Ferrari, R., Griffies, S. M., Hallberg, R. W., Holland, M. M., ... & Samuels, B. L. (2011). Parameterization of mixed layer eddies. III: Implementation and impact in global ocean climate simulations. *Ocean Modelling*, *39*(1-2), 61-78. https://doi.org/10.1016/j.ocemod.2010.09.002

Fox-Kemper, B., Ferrari, R., & Hallberg, R. (2008). Parameterization of mixed layer eddies. Part I: Theory and diagnosis. *Journal of Physical Oceanography*, **38**(6), 1145–1165. https://doi.org/10.1175/2007JPO3792.1

Garfinkel, C. I., White, I., Gerber, E. P., & Jucker, M. (2020). The impact of SST biases in the tropical east Pacific and Agulhas current region on atmospheric stationary waves in the Southern Hemisphere. *Journal of Climate*, 33(21), 9351-9374. https://doi.org/10.1175/JCLI-D-20-0195.1

Gent, P. R., & Mcwilliams, J. C. (1990). Isopycnal mixing in ocean circulation models. *Journal of Physical Oceanography*, **20**, 150–155. https://doi.org/10.1175/1520-0485(1990)020<0150:IMIOCM>2.0.CO;2

Gent, P. R., Yeager, S. G., Neale, R. B., Levis, S., & Bailey, D. A. (2010). Improvements in a half degree atmosphere/land version of the CCSM. *Climate Dynamics*, 34(6), 819-833. https://doi.org/10.1007/s00382-009-0614-8

Good, S. A., Martin, M. J., & Rayner, N. A. (2013). EN4: Quality controlled ocean temperature and salinity profiles and monthly objective analyses with uncertainty estimates. *Journal of Geophysical Research: Oceans*, *118*(12), 6704-6716. https://doi.org/10.1002/2013JC009067

Griffies, S. M., Winton, M., Anderson, W. G., Benson, R., Delworth, T. L., Dufour, C. O., ... & Zhang, R. (2015). Impacts on ocean heat from transient mesoscale eddies in a hierarchy of climate models. *Journal of Climate*, 28(3), 952-977. https://doi.org/10.1175/JCLI-D-14-00353.1

Gutjahr, O., Putrasahan, D., Lohmann, K., Jungclaus, J. H., Storch, J. S. V., Brüggemann, N., ... & Stössel, A. (2019). Max Planck Institute Earth System Model (MPI-ESM1.2) for the High-Resolution Model Intercomparison Project (HighResMIP). *Geoscientific Model Development*, 12(7), 3241-3281. https://doi.org/10.5194/gmd-12-3241-2019

Haarsma, R. J., Roberts, M. J., Vidale, P. L., Senior, C. A., Bellucci, A., Bao, Q., ... & Storch, J. S. V. (2016). High resolution model intercomparison project (HighResMIP v1. 0) for CMIP6. *Geoscientific Model Development*, 9(11), 4185-4208. https://doi.org/10.5194/gmd-9-4185-2016

Haarsma, R., Acosta, M., Bakhshi, R., Bretonnière, P. A., Caron, L. P., Castrillo, M., ... & Wyser, K. (2020). HighResMIP versions of EC-Earth: EC-Earth3P and EC-Earth3P-HR–description, model computational performance and basic validation. *Geoscientific Model Development*, *13*(8), 3507-3527. https://doi.org/10.5194/gmd-2019-350

He, J., & Soden, B. J. (2016). The impact of SST biases on projections of anthropogenic climate change: A greater role for atmosphere-only models?. *Geophysical Research Letters*, 43(14), 7745-7750. https://doi.org/10.1002/2016GL069803

Hieronymus, M., & Nycander, J. (2013). The budgets of heat and salinity in NEMO. *Ocean Modelling*, *67*, 28-38. https://doi.org/10.1016/j.ocemod.2013.03.006

Hsu, W. C., Patricola, C. M., & Chang, P. (2019). The impact of climate model sea surface temperature biases on tropical cyclone simulations. *Climate Dynamics*, 53(1), 173-192. https://doi.org/10.1007/s00382-018-4577-5

Hunke, E. C., & Lipscomb, W. H. (2008). *CICE: the Los Alamos sea ice model user's manual, version 4. Los Alamos National Laboratory Tech. Rep* (pp. 1-76). LA-CC-06-012.

Hyder, P., Edwards, J. M., Allan, R. P., Hewitt, H. T., Bracegirdle, T. J., Gregory, J. M., ... & Belcher, S. E. (2018). Critical Southern Ocean climate model biases traced to atmospheric model cloud errors. *Nature Communications*, 9(1), 1-17. https://doi.org/10.1038/s41467-018-05634-2

Jing, Z., Wang, S., Wu, L., Chang, P., Zhang, Q., Sun, B., ... & Wan, X. (2020). Maintenance of mid-latitude oceanic fronts by mesoscale eddies. *Science Advances*, 6(31), eaba7880. https://doi.org/10.1126/sciadv.aba7880

Johnson, N. C., Krishnamurthy, L., Wittenberg, A. T., Xiang, B., Vecchi, G. A., Kapnick, S. B., & Pascale, S. (2020). The impact of sea surface temperature biases on North American precipitation in a high-resolution climate model. *Journal of Climate*, 33(6), 2427-2447. https://doi.org/10.1175/JCLI-D-19-0417.1

Kirtman, B. P., Bitz, C., Bryan, F., Collins, W., Dennis, J., Hearn, N., ... & Vertenstein, M. (2012). Impact of ocean model resolution on CCSM climate simulations. *Climate Dynamics*, *39*(6), 1303-1328. https://doi.org/10.1007/s00382-012-1500-3

Kurian, J., Li, P., Chang, P., Patricola, C. M., & Small, J. (2021). Impact of the Benguela coastal low-level jet on the southeast tropical Atlantic SST bias in a regional ocean model. *Climate Dynamics*, 1-28. https://doi.org/10.1007/s00382-020-05616-5

Large, W. G., & Danabasoglu, G. (2006). Attribution and impacts of upper-ocean biases in CCSM3. *Journal of Climate*, *19*(11), 2325-2346. https://doi.org/10.1175/JCLI3740.1

Large, W. G., McWilliams, J. C., & Doney, S. C. (1994). Oceanic vertical mixing: A review and a model with a nonlocal boundary layer parameterization. *Reviews of Geophysics*, 32(4), 363-403. https://doi.org/10.1029/94RG01872

Lawrence, D. M., Oleson, K. W., Flanner, M. G., Thornton, P. E., Swenson, S. C., Lawrence, P. J., ... & Slater, A. G. (2011). Parameterization improvements and functional and structural advances in version 4 of the Community Land Model. *Journal of Advances in Modeling Earth Systems*, *3*(1). https://doi.org/10.1029/2011MS00045

Lee, R. W., Woollings, T. J., Hoskins, B. J., Williams, K. D., O'Reilly, C. H., & Masato, G. (2018). Impact of Gulf Stream SST biases on the global atmospheric circulation. *Climate Dynamics*, 51(9), 3369-3387. https://doi.org/10.1007/s00382-018-4083-9

Li, G., & Xie, S. P. (2012). Origins of tropical-wide SST biases in CMIP multi-model ensembles. *Geophysical Research Letters*, *39*(22). https://doi.org/10.1029/2012GL053777

Liu, X., Ma, X., Chang, P., Jia, Y., Fu, D., Xu, G., ... & Patricola, C. M. (2021). Ocean fronts and eddies force atmospheric rivers and heavy precipitation in western North America. *Nature Communications*, *12*(1), 1-10. https://doi.org/10.1038/s41467-021-21504-w

Ma, H. Y., Siongco, A. C., Klein, S. A., Xie, S., Karspeck, A. R., Raeder, K., ... & Tribbia, J. J. (2021). On the correspondence between seasonal forecast biases and long-term climate biases in sea surface temperature. *Journal of Climate*, *34*(1), 427-446. https://doi.org/10.1175/JCLI-D-20-0338.1

McCabe, G. J., Palecki, M. A., & Betancourt, J. L. (2004). Pacific and Atlantic Ocean influences on multidecadal drought frequency in the United

States. *Proceedings of the National Academy of Sciences*, *101*(12), 4136-4141. https://doi.org/10.1073/pnas.0306738101

McGregor, S., Stuecker, M. F., Kajtar, J. B., England, M. H., & Collins, M. (2018). Model tropical atlantic biases underpin diminished pacific decadal variability. *Nature Climate Change*, 8(6), 493-498. https://doi.org/10.1038/s41558-018-0163-4

McPhaden, M. J., Zebiak, S. E., & Glantz, M. H. (2006). ENSO as an integrating concept in earth science. *Science*, *314*(5806), 1740-1745. https://doi.org/10.1126/science.1132588

Meehl, G. A., Yang, D., Arblaster, J. M., Bates, S. C., Rosenbloom, N., Neale, R., ... & Danabasoglu, G. (2019). Effects of model resolution, physics, and coupling on Southern Hemisphere storm tracks in CESM1. 3. *Geophysical Research Letters*, *46*(21), 12408-12416. https://doi.org/10.1029/2019GL084057

Minobe, S., Kuwano-Yoshida, A., Komori, N., Xie, S. P., & Small, R. J. (2008). Influence of the Gulf Stream on the troposphere. *Nature*, *452*(7184), 206-209. https://doi.org/10.1038/nature06690

Moum, J. N., Perlin, A., Nash, J. D., & McPhaden, M. J. (2013). Seasonal sea surface cooling in the equatorial Pacific cold tongue controlled by ocean mixing. *Nature*, *500*(7460), 64-67. https://doi.org/10.1038/nature12363

Neale, R. B., Chen, C. C., Gettelman, A., Lauritzen, P. H., Park, S., Williamson, D. L., ... & Taylor, M. A. (2010). Description of the NCAR community atmosphere model (CAM 5.0). *NCAR Tech. Note NCAR/TN-486+ STR*, *1*(1), 1-12.

Pandey, L. K., & Dwivedi, S. (2021). Comparing the performance of turbulent kinetic energy and k-profile parameterization vertical parameterization schemes over the tropical Indian Ocean. *Marine Geodesy*, *44*(1), 42-69. https://doi.org/10.1080/01490419.2020.1835758

Rayner, N. A. A., Parker, D. E., Horton, E. B., Folland, C. K., Alexander, L. V., Rowell, D. P., ... & Kaplan, A. (2003). Global analyses of sea surface temperature, sea ice, and night marine air temperature since the late nineteenth century. *Journal of Geophysical Research: Atmospheres*, *108*(D14). https://doi.org/10.1029/2002JD002670

Reynolds, R. W., & Smith, T. M. (1994). Improved global sea surface temperature analyses using optimum interpolation. *Journal of Climate*, *7*(6), 929-948. https://doi.org/10.1175/1520-0442(1994)007<0929:IGSSTA>2.0.CO;2

Roberts, C. D., Senan, R., Molteni, F., Boussetta, S., Mayer, M., & Keeley, S. P. (2018). Climate model configurations of the ECMWF Integrated Forecasting System (ECMWF-IFS cycle 43r1) for HighResMIP. *Geoscientific Model Development*, *11*(9), 3681-3712. https://doi.org/10.5194/gmd-11-3681-2018

Roberts, M. J., Baker, A., Blockley, E. W., Calvert, D., Coward, A., Hewitt, H. T., ... & Vidale, P. L. (2019). Description of the resolution hierar-

chy of the global coupled HadGEM3-GC3.1 model as used in CMIP6 HighResMIP experiments. *Geoscientific Model Development*, 12(12), 4999-5028. https://doi.org/10.5194/gmd-12-4999-2019

Roemmich, D., Johnson, G. C., Riser, S., Davis, R., Gilson, J., Owens, W. B., ... & Ignaszewski, M. (2009). The Argo Program: Observing the global ocean with profiling floats. *Oceanography*, *22*(2), 34-43. https://doi.org/10.5670/oceanog.2009.36

Semmler, T., Danilov, S., Rackow, T., Sidorenko, D., Hegewald, J., Sein, D., Wang, Q., & Jung, T. (2017). *AWI AWI-CM 1.1 HR model output prepared for CMIP6 HighResMIP*. Earth System Grid Federation. Retrieved from http://cera-www.dkrz.de/WDCC/meta/CMIP6/CMIP6.HighResMIP.AWI.AWI-CM-1-1-HR

Small, R. J., Bacmeister, J., Bailey, D., Baker, A., Bishop, S., Bryan, F., ... & Vertenstein, M. (2014a). A new synoptic scale resolving global climate simulation using the Community Earth System Model. *Journal of Advances in Modeling Earth Systems*, *6*(4), 1065-1094. https://doi.org/10.1002/2014MS000363

Small, R. J., Curchitser, E., Hedstrom, K., Kauffman, B., & Large, W. G. (2015). The Benguela upwelling system: Quantifying the sensitivity to resolution and coastal wind representation in a global climate model. *Journal of Climate*, 28(23), 9409-9432. https://doi.org/10.1175/JCLI-D-15-0192.1

Small, R. J., Tomas, R. A., & Bryan, F. O. (2014b). Storm track response to ocean fronts in a global high-resolution climate model. *Climate Dynamics*, *43*(3-4), 805-828. https://doi.org/10.1007/s00382-013-1980-9

Smith, R., Jones, P., Briegleb, B., Bryan, F., Danabasoglu, G., Dennis, J., ... & Yeager, S. (2010). The parallel ocean program (POP) reference manual ocean component of the community climate system model (CCSM) and community earth system model (CESM). *LAUR-01853*, *141*, 1-140.

Smith, S. R., Alory, G., Andersson, A., Asher, W., Baker, A., Berry, D. I., ... & Vinogradova-Shiffer, N. (2019). Ship-based contributions to global ocean, weather, and climate observing systems. *Frontiers in Marine Science*, *6*, 434. https://doi.org/10.3389/fmars.2019.00434

Song, X., & Zhang, G. J. (2009). Convection parameterization, tropical Pacific double ITCZ, and upper-ocean biases in the NCAR CCSM3. Part I: Climatology and atmospheric feedback. *Journal of Climate*, *22*(16), 4299-4315. https://doi.org/10.1175/2009JCLI2642.1

Su, Z., Torres, H., Klein, P., Thompson, A. F., Siegelman, L., Wang, J., ... & Hill, C. (2020). High-frequency submesoscale motions enhance the upward vertical heat transport in the global ocean. *Journal of Geophysical Research: Oceans*, *125*(9), e2020JC016544. https://doi.org/10.1029/2020JC016544

Su, Z., Wang, J., Klein, P., Thompson, A. F., & Menemenlis, D. (2018). Ocean

submesoscales as a key component of the global heat budget. *Nature Communications*, *9*(1), 1-8. https://doi.org/10.1038/s41467-018-02983-w

Van Roekel, L., Adcroft, A. J., Danabasoglu, G., Griffies, S. M., Kauffman, B., Large, W., ... & Schmidt, M. (2018). The KPP boundary layer scheme for the ocean: Revisiting its formulation and benchmarking one-dimensional simulations relative to LES. *Journal of Advances in Modeling Earth Systems*, 10(11), 2647-2685. https://doi.org/10.1029/2018MS001336

Vannière, B., Guilyardi, E., Toniazzo, T., Madec, G., & Woolnough, S. (2014). A systematic approach to identify the sources of tropical SST errors in coupled models using the adjustment of initialised experiments. *Climate Dynamics*, *43*(7), 2261-2282. https://doi.org/10.1007/s00382-014-2051-6

Voldoire, A., Saint-Martin, D., Sénési, S., Decharme, B., Alias, A., Chevallier, M., ... & Waldman, R. (2019). Evaluation of CMIP6 deck experiments with CNRM-CM6-1. *Journal of Advances in Modeling Earth Systems*, *11*(7), 2177-2213. https://doi.org/10.1029/2019MS001683

von Storch, J. S., Haak, H., Hertwig, E., & Fast, I. (2016). Vertical heat and salt fluxes due to resolved and parameterized meso-scale eddies. *Ocean Modelling*, *108*, 1-19. https://doi.org/10.1016/j.ocemod.2016.10.001

Wang, C., Zhang, L., Lee, S. K., Wu, L., & Mechoso, C. R. (2014). A global perspective on CMIP5 climate model biases. *Nature Climate Change*, *4*(3), 201-205. https://doi.org/10.1038/nclimate2118

Woelfle, M. D., Yu, S., Bretherton, C. S., & Pritchard, M. S. (2018). Sensitivity of coupled tropical Pacific model biases to convective parameterization in CESM1. *Journal of Advances in Modeling Earth Systems*, *10*(1), 126-144. https://doi.org/10.1002/2017MS001176

Wolfe, C. L., Cessi, P., McClean, J. L., & Maltrud, M. E. (2008). Vertical heat transport in eddying ocean models. *Geophysical Research Letters*, *35*(23). https://doi.org/10.1029/2008GL036138

Woodruff, S. D., Diaz, H. F., Worley, S. J., Reynolds, R. W., & Lubker, S. J. (2005). Early ship observational data and ICOADS. *Climatic Change*, *73*(1), 169-194. https://doi.org/10.1007/s10584-005-3456-3

Wu, P., Roberts, M., Martin, G., Chen, X., Zhou, T., & Vidale, P. L. (2019). The impact of horizontal atmospheric resolution in modelling air–sea heat fluxes. *Quarterly Journal of the Royal Meteorological Society*, *145*(724), 3271-3283. https://doi.org/10.1002/qj.3618

Xu, Z., Chang, P., Richter, I., & Tang, G. (2014). Diagnosing southeast tropical Atlantic SST and ocean circulation biases in the CMIP5 ensemble. *Climate Dynamics*, *43*(11), 3123-3145. https://doi.org/10.1007/s00382-014-2247-9

Ying, J., Huang, P., Lian, T., & Tan, H. (2019). Understanding the effect of an excessive cold tongue bias on projecting the tropical Pacific SST

warming pattern in CMIP5 models. *Climate Dynamics*, *52*(3), 1805-1818. https://doi.org/10.1007/s00382-018-4219-y

Zhang, L., & Zhao, C. (2015). Processes and mechanisms for the model sst biases in the north a tlantic and north pacific: a link with the a tlantic meridional overturning circulation. *Journal of Advances in Modeling Earth Systems*, *7*(2), 739-758. https://doi.org/10.1002/2014MS000415

Zhang, R., Delworth, T. L., Rosati, A., Anderson, W. G., Dixon, K. W., Lee, H. C., & Zeng, F. (2011). Sensitivity of the North Atlantic Ocean circulation to an abrupt change in the Nordic Sea overflow in a high resolution global coupled climate model. *Journal of Geophysical Research: Oceans*, 116(C12). https://doi.org/10.1029/2011JC007240

Zhu, Y., Zhang, R. H., & Sun, J. (2020). North Pacific upper-ocean cold temperature biases in CMIP6 simulations and the role of regional vertical mixing. *Journal of Climate*, 33(17), 7523-7538. https://doi.org/10.1175/JCLI-D-19-0654.1